



저작자표시-비영리-변경금지 2.0 대한민국

이용자는 아래의 조건을 따르는 경우에 한하여 자유롭게

- 이 저작물을 복제, 배포, 전송, 전시, 공연 및 방송할 수 있습니다.

다음과 같은 조건을 따라야 합니다:



저작자표시. 귀하는 원저작자를 표시하여야 합니다.



비영리. 귀하는 이 저작물을 영리 목적으로 이용할 수 없습니다.



변경금지. 귀하는 이 저작물을 개작, 변형 또는 가공할 수 없습니다.

- 귀하는, 이 저작물의 재이용이나 배포의 경우, 이 저작물에 적용된 이용허락조건을 명확하게 나타내어야 합니다.
- 저작권자로부터 별도의 허가를 받으면 이러한 조건들은 적용되지 않습니다.

저작권법에 따른 이용자의 권리는 위의 내용에 의하여 영향을 받지 않습니다.

이것은 [이용허락규약\(Legal Code\)](#)을 이해하기 쉽게 요약한 것입니다.

[Disclaimer](#)

공학박사학위논문

**A Study on the Fracture and  
Deformation Behavior of Ceramics  
in Nanoscale**

세라믹 재료의 나노 스케일에서의  
파괴 및 변형 거동에 대한 연구

**2019년 2월**

서울대학교 대학원

재료공학부

강성규

## **ABSTRACT**

Ceramic materials, which are inorganic compounds of metal, non-metal or metalloid atoms bonded in ionic and covalent bonds, have been essential constituents in the construction, aerospace, automotive, optics, electronics industries due to their superior thermal, corrosion, optical, and electrical properties. However, its low ductility and brittle nature complicate the fabrication process and constantly cause concerns about mechanical reliability of the ceramic structural materials. In order to fabricate a ceramic structural material, complex processes such as glasswork or sintering in high temperature conditions should be involved. Furthermore, these fabrication processes are not suitable for fabricating complex geometries. In addition, flaws are spontaneously generated inside the material, which reduces the fracture strength and arouse an apprehension on the mechanical reliability.

In the virtue of improvements in the fabrication technologies of structural materials, ceramic nanomaterials with superior physical properties also have attracted much attention in biomaterial, energy material, and advanced electronic devices. However, scientific and engineering issues related to the mechanical properties of the ceramic nanomaterials including the low ductility and the brittle fracture still remain unraveled and prevent a lively discussion on the practical applications. Recently, the size-related phenomenon of “smaller is

stronger” in ceramic nanomaterials have been reported, but the nano-flaws inside the material are not considered in previous researches. In addition, the unprecedented ductile deformation of the amorphous silica under the high energy electron-beam irradiation have also been reported. Even though this behavior could be a breakthrough in the fabrication process of the brittle ceramic materials, rigorous study on the electron-beam induced deformation behavior of the ceramic nanomaterials including the crystalline and amorphous phase is still lacking. Therefore, this research investigates the fracture strength of the ceramic nanomaterials containing nano-flaws and the ductile deformation behavior of the ceramic nanomaterials induced by the electron-beam irradiation.

Firstly, the fracture strength of the ceramic nanostructures containing multiple spherical nanopores was evaluated. A ceramic based hollow nanoshell structure have been proposed as an interlayer structure of the GaN LEDs as these structures are able to mitigate the residual thermal stress in GaN thin film and improve the efficiency of the device. However, questions are being asked regarding whether the nanoshell structure can guarantee the mechanical reliability when exposed to the residual thermal stress field in the GaN thin film. In order to address this question, the  $\alpha$ -alumina hollow nanoshell structures were fabricated through a series of processes. With an in-situ mechanical testing and finite element simulations, the high fracture strength of the nanoshell structure (16 GPa) which is four times higher than that of the

conventional bulk  $\alpha$ -alumina was evaluated. This high fracture strength of the  $\alpha$ -alumina nanoshell structure can also be explained in terms of the conventional fracture mechanics where the concentrated stress near theoretical tensile strength is developed around the internal flaw at the moment of the crack formation. Based on the fundamental understanding of the fracture strength of the nanoshell structure, the applicability of the nanoshell structure as the interlayer of the GaN LEDs was investigated through the finite element simulation. From the computational analysis, the mitigation of the residual thermal stress of GaN thin film was confirmed when the nanoshell structure is applied as the interlayer of the GaN LEDs. Most importantly, the mechanical reliability of the nanoshell structure can be secured, with a factor of safety of about 10, owing to the high fracture strength. The mechanically robust nanoshell structure introduced GaN LEDs was successfully fabricated and exhibited an improved output power that is 2.2 times higher than that of conventional GaN LEDs.

Secondly, the ductile deformation behavior of ceramic nanomaterials induced by the electron-beam irradiation was investigated. Rigorous research on the low energy electron-beam induced mechanical softening of the ceramic nanomaterials and its relationship with the electron-beam parameters, such as the acceleration voltage, the beam current, etc. was conducted. It was confirmed that the mechanical softening and plastic deformation of the amorphous silica are activated even under the low energy electron-beam of the SEM. Monte-

carlo simulation on the interaction between the incident electrons and the material suggested that this electron-beam effect strongly depends on the interacting volume between the incident electrons and the material. Moreover, this electron-beam induced deformation behavior was also found in the other amorphous ceramic materials including  $\text{Al}_2\text{O}_3$  and  $\text{TiO}_2$ . Similarity between the electron-beam induced deformation behavior and the thermally activated homogeneous shear flow of the amorphous ceramic materials implied that the incident electrons into the material directly affect the interatomic bond nature, and a deformation behavior mimicking the thermally activated homogeneous shear flow operates under the electron-beam irradiation. In case of the crystalline ceramics, the  $\text{SiO}_2$  is the only ceramic material which exhibits the electron-beam induced deformation behavior, because of its unique atomic structure where the amorphization, phase transformation from crystalline to amorphous phase, occurs under pressure. The electron-beam affected deformation behavior of the crystalline  $\text{SiO}_2$  can be defined as the decrease in amorphization threshold pressure of the crystalline  $\text{SiO}_2$  and the mechanical softening of the amorphized  $\text{SiO}_2$ . Surprising findings on the electron-beam induced deformation behavior allow of performing a glasswork, normally conducted at high temperature for bulk scale, inside the SEM by exerting forces on the ceramic materials with the electron-beam irradiation. The feasibility of the “Nano-glasswork” was demonstrated by forming the silica nanoshell sphere in three different ways. During simple uniaxial loading, multi-axial loading,

and molding into the trench, the silica nanoshell spheres were successfully deformed into the desired shaped without any crack formation.

From this research, fundamental understandings of the fracture strength and the deformation behavior of the ceramic nanomaterials were established. Through the comprehensive study on the fracture strength, it is expected that an invaluable baseline for the design of 3D ceramic nanostructures in advanced devices will be provided. Moreover, an in-depth understanding of the ductile deformation of the ceramic nanomaterials induced by the electron-beam irradiation will be a stepping stone for advanced manufacturing process for ceramic nanomaterials. It is believed that this research will provide a breakthrough in the research on the ceramic structural nanomaterials and pioneer new fields in the fabrication processes and the practical applications.

**Keywords:** Ceramics, Nanostructures, Nanopores, Fracture strength, Size effects, Conventional fracture mechanics, Mechanical reliability, Plastic deformation, Mechanical softening, Electron-beam, Elastic/Inelastic scattering, in-situ Nano-indentation system, SEM, FIB, TEM, Finite element simulation, CASINO monte-carlo simulation, Light-emitting diodes, Formability

**Student number:** 2013-20578

# Contents

<b>Abstract .....</b>	<b>I</b>
<b>Table of Contents .....</b>	<b>VI</b>
<b>List of Tables .....</b>	<b>X</b>
<b>List of Figures .....</b>	<b>XI</b>

## Chapter 1

### Introduction

<b>1.1 Ceramic materials in nanoscale.....</b>	<b>1</b>
<b>1.2 Mechanical properties of ceramic materials.....</b>	<b>3</b>
<b>1.3 Motivations of the thesis .....</b>	<b>5</b>
<b>1.4 References .....</b>	<b>7</b>



## Chapter 2

### Fracture behavior of ceramic nanomaterials with nano-flaws

<b>2.1 Introduction</b> .....	12
<b>2.2 <math>\alpha</math>-Alumina nanoshell structure</b> .....	15
2.2.1 Specimen preparation .....	15
2.2.2 Structural characterization .....	19
<b>2.3 Fracture strength of <math>\alpha</math>-Alumina nanoshell structure</b> .....	24
2.3.1 Experimental results .....	25
2.3.2 Computational results .....	29
2.3.3 Fracture strength and fracture criteria of the $\alpha$ -alumina nanoshell structure .....	35
<b>2.4 Applicability of 3D ceramic nanostructure</b> .....	42
2.4.1 Mechanical reliability of the nanoshell structure .....	43
2.4.2 GaN LEDs incorporated with the nanoshell structure .....	47

<b>2.5 Conclusion</b> .....	49
<b>2.6 References</b> .....	50

## **Chapter 3**

### **Ductile deformation behavior of ceramic nanomaterials induced by electron-beam irradiation**

<b>3.1 Introduction</b> .....	53
<b>3.2 Materials and methods</b> .....	56
3.2.1 Specimen preparation .....	56
3.2.2 Experimental methods .....	59
<b>3.3 Electron-beam effect on deformation behavior of amorphous ceramics</b> .....	61
3.3.1 E-beam effect on deformation behavior of amorphous silica ...	61
3.3.2 Interaction between the incident electrons and the amorphous silica sphere .....	71

3.3.3 E-beam effect on deformation behavior of other amorphous ceramics .....	85
<b>3.4 Electron-beam effect on deformation behavior of crystalline ceramics .....</b>	<b>88</b>
3.4.1 E-beam effect on deformation behavior of crystalline ceramics .....	89
3.4.2 Correlation between E-beam affected deformation behavior and atomic structure of crystalline ceramics .....	99
<b>3.5 Nano-glasswork of ceramic nanomaterials utilizing Electron-beam irradiation .....</b>	<b>104</b>
<b>3.6 Conclusion .....</b>	<b>107</b>
<b>3.7 References .....</b>	<b>109</b>
<b>Chapter 4</b>	
<b>Total conclusion.....</b>	<b>113</b>

## **LIST OF TABLES**

Table 2.1 Radius and position of the chosen-nanopores and the critical nanopore.

Table 3.1 E-beam conditions for in-situ compression tests.

# LIST OF FIGURES

Figure 1.1 Young's modulus, Strength and Elongation diagram of the materials including metals, polymers, rubbers, and ceramics. Well-known ceramics such as  $\text{SiO}_2$  and  $\text{Al}_2\text{O}_3$  are highlighted with asterisks.

Figure 2.1 Sample preparation using photolithography, atomic layer deposition, and thermal treatment.

Figure 2.2 Thermal gravimetric analysis of the photoresist.

Figure 2.3 Cylinder-shaped  $\alpha$ -alumina hollow nanoshell structures. (a) Tilted-view SEM image of 73-nm thickness hollow nanoshell structure. (b) Cross-sectional TEM image of 73-nm thickness hollow nanoshell structure. (c, d) Magnified TEM images of area indicated with red and orange squares in b. Insets show SAED patterns of the area marked with white circles in each figure. (e) Distribution of radius of nanopores inside each nanoshell: 63-nm thickness nanoshell (top), 73-nm thickness nanoshell (middle), and 115-nm thickness

nanoshell (bottom).

Figure 2.4 Analysis of the nanopore distributions in each nanoshell with thickness of 63 nm, 73 nm, and 115 nm. (a) Tilted-view SEM images (500 nm scale bars) and (b) cross-sectional TEM images (100 nm scale bars) of CSH nanoshell structures with thickness of 63, 73, and 115 nm, as indicated. The red and yellow circles indicate nanopores inside the nanoshells. (c) Radii distribution of the nanopores inside each nanoshell obtained from the SEM images. (d) Position distribution of the nanopores inside each nanoshell obtained from the TEM images.

Figure 2.5 In-situ indentation test of 73-nm thickness CSH nanoshell structure. (a-e) Series of SEM images of in-situ indentation. (f) Load-displacement (L-D) curve of 300-nm indentation. (g) L-D curve of 100-nm indentation. Inset indicates load function. (h, i) Top-view SEM images of 73-nm thickness CSH nanoshell structure. The yellow circle and white arrows represent the contact

area of the indenter tip and the deformation-induced cracks, respectively. SEM images with colored frames (b-d), (h-i) represent the tilted- and top-view SEM images of 73-nm thickness CSH nanoshell structures at each point marked with circles of the same color on the 300-nm indentation L-D curve (f). The scale bars are 1  $\mu\text{m}$ .

Figure 2.6 Load-displacement curves from in-situ indentation tests for each hollow nanoshell structure with shell thickness of 63 nm (blue), 73 nm (red), and 115 nm (black). The solid arrows and hollow arrows indicate crack initiation and structural collapse, respectively.

Figure 2.7 Representation of the computational model for in-situ indentation tests. The light green, orange, and gray sections indicate the  $\alpha$ -alumina hollow nanoshell structures, sapphire substrate, and cono-spherical indenter, respectively. The blue triangles indicate the boundary conditions.

Figure 2.8 Load-displacement curves of the finite element simulations using an

anisotropic model with elastic constants for the alpha alumina (green) and an isotropic model with elastic modulus of 425 GPa (orange).

Figure 2.9 Average indentation depth where crack initiates for each hollow nanoshell structure with shell thickness of 63, 73, and 115 nm, as indicated.

Figure 2.10 Finite element analysis of in-situ indentation tests for CSH nanoshell structures. (a-c) Representative experimental L-D curves of 63-nm thickness (a), 73-nm thickness (b), and 115-nm thickness (c) CSH nanoshell structures and corresponding FE simulations (red line). The black and gray points represent the material response before and after the crack initiation, respectively. (d-left) Cut-view of meshes used in FE simulation. The green, orange, and gray elements indicate the  $\alpha$ -alumina hollow nanoshell structures, sapphire substrate, and indenter tip, respectively. (d-right) Maximum principal stress distribution within each CSH nanoshell structure. The nanoshell is



assumed to be solid. (e) Maximum principal stress distribution around critical nanopore for each CSH nanoshell structure.

Figure 2.11 Representation of the computational model for evaluating stress evolution near the nanopores. The light-blue section represents the stress concentration part that contains the critical nanopore and  $\alpha$ -alumina matrix, and the green sections represent the other  $\alpha$ -alumina matrix, which is assumed a solid with an effective elastic modulus.

Figure 2.12 Representation of the computational model of (a) conventional GaN LEDs and (b)  $\alpha$ -alumina hemispherical hollow nanoshell structure-incorporated GaN LEDs. The gray, green, and dark-blue areas indicate the GaN thin film, hollow nanoshell structures, and sapphire substrate, respectively.

Figure 2.13 Introduction of hemisphere-shaped  $\alpha$ -alumina hollow nanoshell structures to GaN LEDs. (a) Tilted-view SEM image of HSH nanoshell structure (top) and cross-sectional SEM image of HSH nanoshell structure

(bottom) after GaN thin film deposition. Scale bar is 1  $\mu\text{m}$ . (b) Residual stress distribution within GaN thin film and sapphire substrate of conventional (left) and HSH nanoshell structure-incorporated (right) GaN LEDs when cooling from 1040  $^{\circ}\text{C}$  to 25  $^{\circ}\text{C}$  ends. (c) Maximum principal stress evolution of inner nanoshell structure (top) and outer nanoshell structure (bottom) when cooling from 1040  $^{\circ}\text{C}$  to 25  $^{\circ}\text{C}$  ends.

Figure 2.14 Schematic diagrams and turn-on images of conventional (left) and HSH nanoshell structures-incorporated (right) GaN LEDs with average light output power of the LED chips with HSH nanoshell structures (red spheres) and without HSH nanoshell structures (black squares).

Figure 3.1 Diameter distribution of the amorphous silica spheres.

Figure 3.2 SEM images of the amorphous silica sphere before and after compression under various e-beam conditions. (a) Compressed amorphous silica spheres up to various indentation depths with/without the e-beam. (b)

Compressed amorphous silica spheres up to  $100\mu\text{N}$  under various e-beam conditions. Scale bars indicate 200 nm.

Figure 3.3 Load-indentation depth curves of the amorphous silica sphere compression test up to  $100\mu\text{N}$  under various e-beam conditions.

Figure 3.4 Load-indentation depth curves of the amorphous silica sphere compression test up to  $20\mu\text{N}$  with/without the E-beam. Black and red color indicates the results without and with the E-beam, respectively.

Figure 3.5 Softness parameters of the amorphous silica spheres calculated from the load-displacement curve of the compression tests under the various e-beam conditions.

Figure 3.6 In-situ compression tests of the fused silica pillar under the e-beam with 5 kV acceleration voltage. (a) Engineering stress-Engineering strain curves of the compression tests. (b) SEM images of the compressed pillars. (c) Plotted normalized softness parameters of the compressed fused quartz pillars

with those of the compressed amorphous silica sphere. Scale bars indicate 200 nm.

Figure 3.7 Interaction between the incident electrons and the amorphous silica sphere. (a) Absorbed energies by the amorphous silica sphere from the e-beam. (b) Non-interacting volume fractions inside the amorphous silica sphere under the various e-beam conditions. (c) Interacting volume induced by 13 pA E-beam as viewed from the cross-section of the amorphous silica sphere. (d) Interacting volume induced by 5 kV 100 pA E-beam as viewed from the cross-section of the amorphous silica sphere. Interacting and non-interacting area are indicated as yellow and blue color, respectively.

Figure 3.8 Scan rate dependency of the E-beam induced deformation behavior of the silica pillars. Engineering stress-engineering strain curves of the compression tests under the E-beam of 5 kV (a) and 18 kV (b) acceleration voltage.

Figure 3.9 Pixel size dependency of the E-beam induced deformation behavior of the silica pillars. Engineering stress-engineering strain curves of the compression tests under the E-beam of 5 kV (a) and 18 kV (b) acceleration voltage.

Figure 3.10 Load-displacement of the in-situ compression test of the amorphous silica nanoshell sphere with/without the E-beam. Insets indicate the SEM images of the compressed nanoshell spheres.

Figure 3.11 Engineering stress-engineering strain curves of the in-situ compression test of fused quartz pillars at 0.0006, 0.002, 0.006, 0.014 s<sup>-1</sup> strain rate under (a) beam off , (b) 2 kV E-beam, (c) 5 kV E-beam, and (d) 18 kV E-beam conditions

Figure 3.12 Compression test with various strain rates under 2 kV, 5 kV, 18 kV acceleration voltage e-beams. (a) Strain rate sensitivity and (b) activation volume plot of the fused quartz pillars. Black, orange, green, blue colors

indicate compression test under no e-beam, 2 kV, 5 kV, and 18 kV acceleration voltage e-beam respectively.

Figure 3.13 Engineering stress-engineering strain curves of the in-situ compression test of amorphous ceramics: (a) amorphous  $\text{Al}_2\text{O}_3$ , (b) amorphous  $\text{TiO}_2$ . Insets indicate the compressed amorphous ceramic pillars.

Figure 3.14 Engineering stress-engineering strain curves of the in-situ compression test of crystalline ceramics: (a) crystalline  $\text{Al}_2\text{O}_3$ , (b) crystalline  $\text{TiO}_2$ , (c) crystalline  $\text{ZnO}$  Insets indicate the compressed amorphous ceramic pillars.

Figure 3.15 Engineering stress-engineering strain curves of the in-situ compression tests of the c- $\text{SiO}_2$  pillars under the 5 kV e-beam.

Figure 3.16 SEM images of the compressed c- $\text{SiO}_2$  pillars under the 5 kV e-beam. Scale bar indicates 200 nm.

Figure 3.17 TEM dark field images of the compressed c-SiO<sub>2</sub> pillars under the 5 kV e-beam. Bright white and dark area indicate the crystalline and the amorphous phase, respectively.

Figure 3.18 In-situ compression test of the crystalline SiO<sub>2</sub> pillar under 5 kV 0.4 nA e-beam. (a) Corresponding engineering stress-engineering strain curve. (b) Snap shot of the crystalline SiO<sub>2</sub> pillar before compression test. (c) Snap shot at each strain during the in-situ compression test.

Figure 3.19 Engineering stress-engineering strain curves of the in-situ compression tests of the crystalline SiO<sub>2</sub> pillar under 5 kV 0.4 nA e-beam up to various maximum strains.

Figure 3.20 TEM dark field images of the compressed c-SiO<sub>2</sub> pillars under the 5 kV e-beam up to various maximum strains. Bright white and dark area indicate the crystalline and the amorphous phase, respectively. Scale bars indicate 200 nm.

Figure 3.21 Amorphization threshold stress analysis. (a) Engineering stress-engineering stress curve of the crystalline SiO<sub>2</sub> pillar compressed without the e-beam. Red dotted line indicate the stress-strain curve of the crystalline SiO<sub>2</sub> pillar assumed to be linearly elastic. Insets indicate corresponding TEM dark field images at each strains. (b) Pressure distribution when the experimental stress-strain curve deviates from the linearly elastic-assumed curve.

Figure 3.22 Plot of amorphization threshold hydrostatic pressure of the crystalline SiO<sub>2</sub> with beam current of the e-beam.

Figure 3.23 Nano-glasswork of the amorphous silica nanoshell sphere utilizing the E-beam irradiation. (a) Schematic diagram of the nano-glasswork with three different deformation methods. (b) Snap shots during the nano-glasswork by applying multi-axial loads to the nanoshell sphere with nano-manipulators. Scale bar indicate 1  $\mu\text{m}$ . (c) Snap shots during the nano-glasswork by molding the nanoshell sphere into the trench. Scale bar indicate 500 nm.



# Chapter 1

## Introduction

### 1.1 Ceramic materials in nanoscale

Ceramic materials are inorganic compounds of metal, non-metal or metalloid atoms bonded in ionic and covalent bonds.  $\text{SiO}_2$ ,  $\text{SiN}_4$ ,  $\text{Al}_2\text{O}_3$ , and  $\text{TiO}_2$  are the most well-known and widely used ceramic materials. Ceramic materials are structurally either crystalline or amorphous phase (glass ceramics). The crystallinity strongly depends on the heat treatment during the fabrication processes [1-3]. The excellent thermal, corrosion, optical, and electrical properties of the ceramic materials make these materials as core elements in a wide range of industries including construction, aerospace, automotive, electronics, telecommunications etc [4-8].

In recent years, advances in manufacturing technologies have enabled the production of the ceramic materials in nanoscale [9, 10]. Nano-ceramic materials with superior physical properties pave the way for applying the ceramics again not only to existing industries but also new promising fields. Bio-ceramics, which have been used as an artificial bone based on its biocompatibility, have received much attention recently in the field of drug delivery systems. In the form of the porous nanosphere or nanocapsule, the bio-

ceramics can transport the drugs to the target site in the human body and release it at appropriate moment [11-15]. Moreover, in the field of energy materials, researches on applying these ceramic based-capsule structures as an energy harvesting layer in the solar cell and also in the fuel cell have proposed [16-20]. In case of the electric device field, ceramics are widely used as the core functional materials. With the tendency toward higher levels of integration and improvements in the performance of the devices, many research groups are trying to introduce three-dimensional ceramic nanostructures to the device design [21-28]. The growth of the nano-ceramic field is boosting the innovation of the engineering industries, and large potential for further application is expected in the future.

## **1.2 Mechanical properties of ceramic materials**

The physical properties of the ceramic materials can be characterized as a brittleness. As shown in Fig. 1.1, the ceramics materials have higher elastic modulus and tensile strength compared to metals or polymers, while exhibiting a relatively low ductility. The amorphous and crystalline ceramics possess the shear flow and the dislocation slip as the plastic deformation mechanisms, respectively. However, due to their high activation energies, the plastic deformation rarely occurs in the ambient conditions. That is, the ceramic materials only exhibit the brittle fracture when subjected to stress, unless placed at a high temperature condition. Moreover, when the ceramic materials are subjected to an external stress, the local stresses around internal flaw can be concentrated and dramatically extenuated to a level where a catastrophic failure can occur without any warning. However, when fabricating bulk ceramic structural materials, the formation of flaws, with sizes in the order of tens of micrometers, is inevitable. Hence, the fracture strength of conventional ceramic structural materials is only about  $1/10 \sim 1/200$  of their theoretical strength [1, 29, 30]. With high temperatures around  $1000\text{ }^{\circ}\text{C}$ , the crystalline ceramics deforms plastically through dislocation nucleation and migration. For the amorphous ceramics, the homogeneous shear flow can be activated when the temperature reaches the glass transition temperature [1, 3, 29].

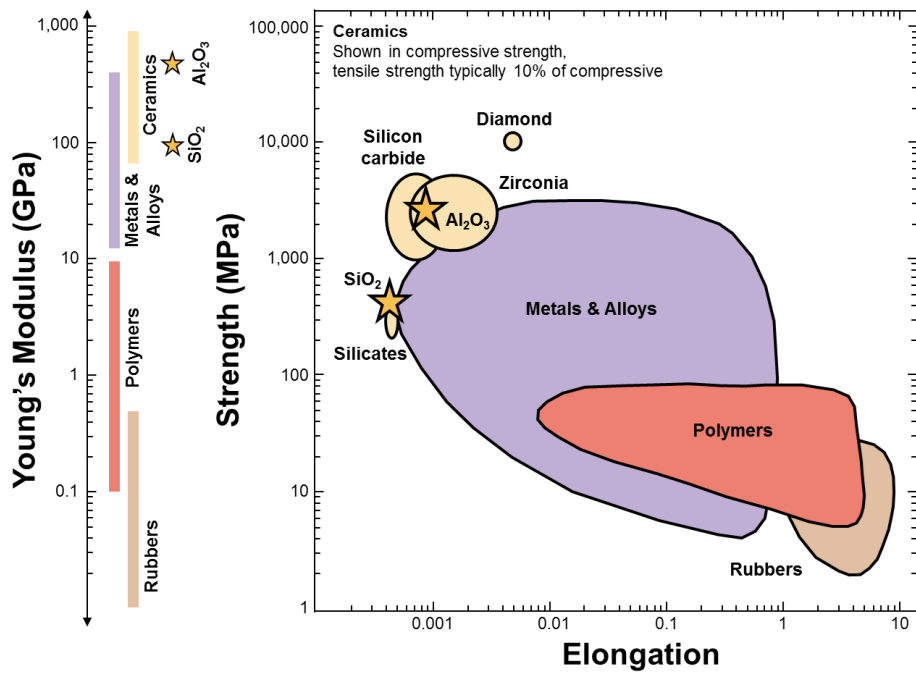


Figure 1.1 Young's modulus, Strength and Elongation diagram of the materials including metals, polymers, rubbers, and ceramics. Well-known ceramics such as SiO<sub>2</sub> and Al<sub>2</sub>O<sub>3</sub> are highlighted with asterisks.

### **1.3 Motivations of the thesis**

Since the nano-ceramic materials also exhibit the brittle properties and the internal defects inevitably appears [31, 32], the fracture behavior and the low plasticity are the biggest obstacles for applying the nanoceramics in the vast engineering fields. These issues not only complicate the fabrication processes of the nano-ceramic structural materials, but also deteriorate the mechanical reliability during the fabrication processes and operation of the device. Recently, the size-related phenomenon of “smaller is stronger”, whereby there is an increase in the strength of metallic materials at the nanoscale [33-39], has also been identified in ceramic materials [31, 40-44]. However, since the most researches focused on the intrinsic fracture strength of the ceramic nanowhiskers, researches on the evaluation of the fracture strength considering flaws, which appear spontaneously inside the nano-ceramic structural materials, is lack.

In Chapter 2, the fracture strength of the crystalline  $\text{Al}_2\text{O}_3$  nanoshell structures containing a significant number of nanopores is evaluated. Furthermore, the fracture behavior is investigated in the point view of the conventional bulk scale fracture mechanics. Based on the evaluated fracture strength of the crystalline  $\text{Al}_2\text{O}_3$  nanoshell structures, the mechanical reliability is also examined when these nanoshell structures are applied into the actual device, GaN light-emitting diodes.

Another issue, the low plasticity of the nano-ceramic materials, is investigated from a different point of view. Recent research have made a breakthrough in the plasticity of nano-ceramic materials by utilizing an electron-beam (henceforth, referred to as “E-beam”) irradiation. Amorphous silica spheres of submicron size exhibit mechanical softening and substantial permanent deformation when deformed under the E-beam irradiation [45-49]. However, rigorous study on these unprecedented phenomenon is still lack as the previous researches only confirmed the possibility of the phenomenon from limited materials, amorphous silica.

In Chapter 3, parametric study on the E-beam induced deformation behavior is achieved by asking questions on the correlation between the factors affecting the E-beam and the related phenomenon. In addition, the E-beam induced ductile deformation behavior of other ceramic materials, including the amorphous and crystalline nano-ceramics, is investigated. Finally, new fabrication process of the nano-ceramic structural material based on the improved ductility, is suggested.

Lastly, total conclusion is addressed in Chapter 4.

## 1.4 References

- [1] Y.-M. Chiang, D.P. Birnie, W.D. Kingery, *Physical Ceramics: Principles for Ceramic Science and Engineering*, Wiley (1997).
- [2] M.N. Rahaman, *Ceramic Processing and Sintering*, 2nd ed., CRC Press (2003).
- [3] W.D. Callister, *Materials Science and Engineering: an Introduction*, Wiley (2013).
- [4] A. Bennett, *Materials Science and Technology*, 2 (1986) 895-899.
- [5] E.G. Butler, *International Journal of High Technology Ceramics*, 4 (1988) 93-102.
- [6] R.C. Buchanan, *Ceramic Materials for Electronics*, 3rd ed., CRC Press (2004).
- [7] X. Zhang, H. Ma, J. Lucas, Y. Guimond, S. Kodjikian, *Journal of Non-Crystalline Solids*, 336 (2004) 49-52.
- [8] N.P. Padture, *Nat Mater*, 15 (2016) 804-809.
- [9] P. Greil, *Adv. Eng. Mater.*, 4 (2002) 247-254.
- [10] A.D. Lantada, A.d.B. Romero, M. Schwentenwein, C. Jellinek, J. Homa, *Smart Materials and Structures*, 25 (2016).
- [11] S. Oh, N. Oh, M. Appleford, J.L. Ong, *American Journal of Biochemistry and Biotechnology*, 2 (2006) 49-56.
- [12] M. Colilla, M. Manzano, M. Vallet-Regi, *International Journal of*

- Nanomedicine, 3 (2008) 403-414.
- [13] L. Yang, B.W. Sheldon, T.J. Webster, American Ceramic Society Bulletin, 89 (2010) 24-32.
- [14] S. Samavedi, A.R. Whittington, A.S. Goldstein, Acta Biomater., 9 (2013) 8037-8045.
- [15] S.C. Thomas, Harshita, P.K. Mishra, S. Talegaonkar, Current Pharmaceutical Design, 21 (2015) 6165-6188.
- [16] Y. Yao, J. Yao, V.K. Narasimhan, Z. Ruan, C. Xie, S. Fan, Y. Cui, Nat. Commun., 3 (2012) 664.
- [17] H. Lv, S. Mu, Nanoscale, 6 (2014) 5063-5074.
- [18] E. Baquedano, L. Torne, P. Cano, P.A. Postigo, Nanomaterials, 7 (2017).
- [19] S.M. Wong, H.Y. Yu, J.S. Li, Y.L. Li, N. Singh, P.G.Q. Lo, D.L. Kwong, IEEE ELECTRON DEVICE LETTERS, 32 (2011) 176-178.
- [20] W. Liu, S.W. Lee, D. Lin, F. Shi, S. Wang, A.D. Sendek, Y. Cui, Nature Energy, 2 (2017).
- [21] X.G. Zheng, H.L. Wang, Q. Gong, L. Chen, K. Wang, S.M. Wang, Materials Letters, 126 (2014) 71-74.
- [22] J. Jang, D. Moon, H.-J. Lee, D. Lee, D. Choi, D. Bae, H. Yuh, Y. Moon, Y. Park, E. Yoon, Journal of Crystal Growth, 430 (2015) 41-45.
- [23] M.K. Kim, D.W. Kim, D.W. Shin, S.J. Seo, H.K. Chung, J.B. Yoo, Phys Chem Chem Phys, 17 (2015) 2416-2420.
- [24] J. Limongelli, F. Tolea, M. Valeanu, L. Diamandescu, T. Xu, M. Sorescu,



- Ceramics International, 41 (2015) 333-343.
- [25] C. Xu, B.M. Gallant, P.U. Wunderlich, T. Lohmann, J.R. Greer, ACS Nano, 9 (2015) 5876-5883.
- [26] Y.J. Moon, D. Moon, J. Jang, J.Y. Na, J.H. Song, M.K. Seo, S. Kim, D. Bae, E.H. Park, Y. Park, S.K. Kim, E. Yoon, Nano Lett, 16 (2016) 3301-3308.
- [27] Z. Dong, J. Ho, Y.F. Yu, Y.H. Fu, R. Paniagua-Dominguez, S. Wang, A.I. Kuznetsov, J.K.W. Yang, Nano Letters, 17 (2017) 7620-7628.
- [28] D.S. Shin, T.G. Kim, D. Kim, K. K.-K, J. Park, Journal of Nanoscience and Nanotechnology, 17 (2017) 4073-4077.
- [29] T.H. Courtney, Mechanical behavior of Materials, McGraw-Hill (2000).
- [30] B.S. Mitchell, An Introduction to Materials Engineering and Science for Chemical and Materials Engineers, Wiley (2004).
- [31] S. Wang, Y. He, H. Huang, J. Zou, G.J. Auchterlonie, L. Hou, B. Huang, Nanotechnology, 24 (2013) 285703.
- [32] M. Vahtrus, M. Umalas, B. Polyakov, L. Dorogin, R. Saar, M. Tamme, K. Saal, R. Löhmus, S. Vlassov, Materials Characterization, 107 (2015) 119-124.
- [33] M.D. Uchic, D.M. Dimiduk, J.N. Florando, W.D. Nix, SCIENCE, 305 (2004) 986-989.
- [34] G. Richter, K. Hillerich, D.S. Gianola, R. Monig, O. Kraft, C.A. Volkert, Nano Lett, 9 (2009) 3048-3052.

- [35] H.S. Park, W. Cai, H.D. Espinosa, H. Huang, *MRS Bulletin*, 34 (2011) 178-183.
- [36] J.H. Seo, H.S. Park, Y. Yoo, T.Y. Seong, J. Li, J.P. Ahn, B. Kim, I.S. Choi, *Nano Lett*, 13 (2013) 5112-5116.
- [37] J. Wang, F. Sansoz, J. Huang, Y. Liu, S. Sun, Z. Zhang, S.X. Mao, *Nat Commun*, 4 (2013) 1742.
- [38] L.Y. Chen, M.R. He, J. Shin, G. Richter, D.S. Gianola, *Nat Mater*, 14 (2015) 707-713.
- [39] B.H. An, I.T. Jeon, J.H. Seo, J.P. Ahn, O. Kraft, I.S. Choi, Y.K. Kim, *Nano Lett*, 16 (2016) 3500-3506.
- [40] G.D. Quinn, P. Green, K. Xu, *J. Am. Ceram. Soc.*, 86 (2003) 441-448.
- [41] Z.W. Shan, G. Adesso, A. Cabot, M.P. Sherburne, S.A. Asif, O.L. Warren, D.C. Chrzan, A.M. Minor, A.P. Alivisatos, *Nat Mater*, 7 (2008) 947-952.
- [42] D. Jang, L.R. Meza, F. Greer, J.R. Greer, *Nat Mater*, 12 (2013) 893-898.
- [43] J. Bauer, S. Hengsbach, I. Tesari, R. Schwaiger, O. Kraft, *Proc Natl Acad Sci U S A*, 111 (2014) 2453-2458.
- [44] J. Luo, J. Wang, E. Bitzek, J.Y. Huang, H. Zheng, L. Tong, Q. Yang, J. Li, S.X. Mao, *Nano Lett*, 16 (2016) 105-113.
- [45] K. Zheng, C. Wang, Y.Q. Cheng, Y. Yue, X. Han, Z. Zhang, Z. Shan, S.X. Mao, M. Ye, Y. Yin, E. Ma, *Nat Commun*, 1 (2010) 24.
- [46] M. Mačković, F. Niekieł, L. Wondraczek, E. Spiecker, *Acta Materialia*, 79 (2014) 363-373.

- [47] M. Mačković, F. Niekieł, L. Wondraczek, E. Bitzek, E. Spiecker, *Scripta Materialia*, 121 (2016) 70-74.
- [48] J. Su, X. Zhu, *RSC Advances*, 7 (2017) 43047-43051.
- [49] J. Su, X. Zhu, *RSC Adv.*, 7 (2017) 45691-45696.

## **Chapter 2**

# Fracture behavior of ceramics with nano-flaws in nanoscale

### **2.1 Introduction**

Strength of nano-ceramic materials has always been questioned because of inherent flaws inside. Flaws in the body or on the surface of bulk ceramic structural materials inevitably appears during fabrication process, and these are regarded as being possible causes of fatal failures because of the stress concentration field around them. Due to these defects, it is always necessary to predict and ensure high fracture strength through control and diagnosis of defects in ceramic structural materials. This research addresses the aforementioned conventional fracture issue at the nanoscale regime, thus raising the issue of whether ceramic nanostructures with internal flaws are strong enough to use as the component advanced electronic and optical devices, more specifically, GaN light-emitting devices (LEDs).

In GaN-based LEDs, the different material properties of the GaN and sapphire lead to several problems such as a high defect density in the GaN, serious wafer bowing in large-area wafers, and poor light extraction in devices [1-3]. These problems can be resolved by introducing a few different types of

hollow oxide nanostructures (silica, alumina, and so forth) into the interface between the GaN thin film and the sapphire substrate [4-6]. Moreover, well-defined hollow nanostructures embedded at the GaN/sapphire interface can help scatter light effectively to attain improved light extraction [5, 6]. However, the formation of internal flaws, especially nanopores, can hardly be avoided during the fabrication or post-treatment process which would be a serious reliability issue because structural failure can occur due to the thermal stress that arises during the fabrication process. Therefore, when applying ceramic nanostructures to novel electronics and optical devices, it is essential to accurately estimate the fracture strength of nanoceramics with internal flaws, which also constitutes a fundamental scientific challenge in the field of nanomechanics.

Even though the “smaller is stronger” phenomenon also recently been reported in ceramic materials, the reason for the phenomenon occurring in nanoceramics has yet to be elucidated. One of the most plausible explanation is that the fracture strength ( $\sigma_F$ ) in the nanoceramic material still depends on the size of the flaw ( $a$ ), which can be roughly estimated to be  $\sigma_F \sim 1/a$ , according to continuum-based fracture mechanics. In other words, the fracture strength drastically increases because the size of the flaw decreases to the nanoscale regime as the size of the specimen reaches the nanoscale level. Nonetheless, it has not yet been clarified whether the fracture strength at the nanoscale level

increases and whether this can be predicted by conventional bulk-scale fracture mechanics. Furthermore, a systematic analysis of the correlation between the fracture strength and there internal flaws, especially the nanopores inside the nanostructure, is still lacking.

In this chapter, it is confirmed that a ceramic nanostructure can exhibit an ultrahigh fracture strength even though it contains a significant number of nanopores. By systematically performing in-situ mechanical testing and finite element simulations, the high fracture strength of  $\alpha$ -alumina hollow nanoshell structure can be explained in terms of conventional fracture mechanics in that the position and size of the nanopores are the most critical factors determining the fracture strength, even at the nanoscales. More importantly, by deriving a fundamental understanding, we would be able to lay down predictions and guidelines for the design of reliable ceramic nanostructures for advanced GaN LEDs. To that end, we demonstrated how our ultra-strong  $\alpha$ -alumina hollow nanoshell structures could be successfully incorporated into GaN LEDs, thereby greatly improving the luminous efficiency and output power of the LEDs [5].

## 2.2 $\alpha$ -Alumina nanoshell structure

### 2.2.1 Specimen preparation

Among the various  $\alpha$ -alumina hollow nanoshell structures of GaN LEDs, a cylinder-shaped hollow nanoshell structure (henceforth, referred to as “CSH nanoshell structure”) was chosen as a model structure because the cylindrical shape is better suited to mechanical testing and analysis than other shapes, while it is also a candidate for application to new GaN LEDs through a conventional fabrication process [5].

A cylindrical photoresist (PR) of 2  $\mu\text{m}$  height and 2  $\mu\text{m}$  diameter was fabricated on a (0001) sapphire substrate using photolithography with a circular hole-patterned mask (Fig. 2.1). Afterwards, an amorphous alumina layer was deposited on the substrate using atomic layer deposition (ALD) using H<sub>2</sub>O and trimethylaluminium as oxygen and aluminum sources, respectively. To maintain the shape of the PR pattern, the temperature was set at 110 °C. To investigate the thickness-dependent size effect on the mechanical properties, the number of deposition cycles was 800, 1000, and 1500 for hollow nanoshell structures of 63, 73, and 115 nm shell thickness, respectively. For the calcination of PR and the crystallization of alumina, heat treatments were performed at 850 °C for 1 h and 1100 °C for 10 h in air, respectively. The PR was composed of an organic solvent and a light-sensitive polymer that can be removed with a reaction with oxygen. The porosity of amorphous alumina

allows oxygen to diffuse so that a reaction with the PR during annealing in ambient air is possible. Gas by-products, such as CO<sub>2</sub>, can be out-diffused through the porous amorphous alumina. Thermal gravimetric analysis of the PR clearly shows that the majority of chemical reactions with oxygen occurred below 600 °C (Fig. 2.2).



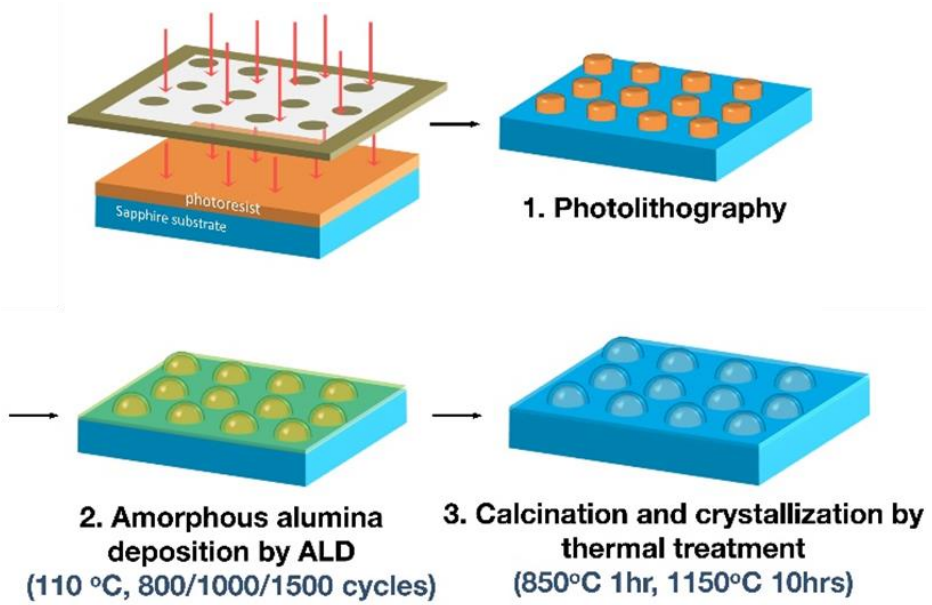


Figure 2.1 Sample preparation using photolithography, atomic layer deposition, and thermal treatment.

## Thermal Gravimetric Analysis (TGA)

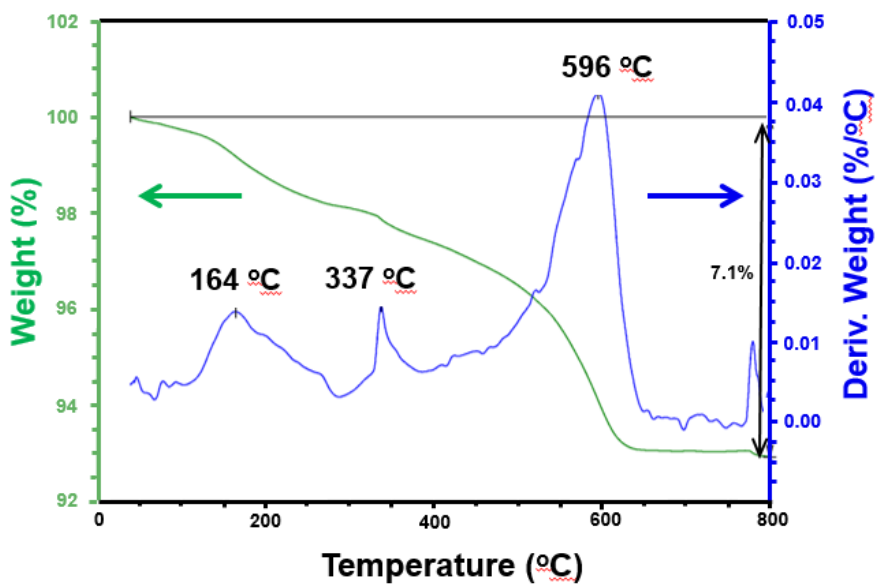


Figure 2.2 Thermal gravimetric analysis of the photoresist.

### 2.2.2 Structural characterization

Fig. 2.3 (a) shows a representative array of CSH nanostructures with a shell thickness of 73 nm on a sapphire wafer. The cross-sectional TEM image of the CSH nanoshell structure in Fig. 2.3 (b) clearly indicates that the CSH nanoshell structures retained a hollow alumina wall while the residual photoresist inside the nanoshell was burned away during the heat treatment. (Note that the space inside of the CSH nanoshell structure is partly filled with Ga residue from focused ion beam sampling.). The TEM analysis shown in Fig. 2.3 (c) and (d) confirm that the as-deposited alumina, which was originally amorphous, crystallized to the  $\alpha$  phase as a result of the heat treatment. This phase is the same as that of the sapphire wafer. Moreover, diffraction patterns in Fig. 2.3 (c) and (d) show that the  $\alpha$ -alumina nanoshell is a single crystalline solid having the same crystallographic orientation with the (0001) sapphire substrate.

More importantly, the fabricated CSH nanoshell structures contained multiple spherical nanopores. To analyze the nanopore distribution, we combined 2D SEM images with the cross-section TEM images of each CSH nanoshell structure. Fig. 2.4 (a) and (b) show the SEM and cross-section TEM images, respectively, confirming the presence of nanopores in the structures. Specifically, the nanopores' presence is expressed as the contrast difference in the SEM images because of the low interaction between the material and the electrons at the nanopore. This methodology allowed us to extract simply the

porosity of each CSH nanoshell structure and the nanopore distribution without using a 3D tomography tool.

2D porosities of each CSH nanoshell structure were extracted from the area ratio between the nanopores (express as dark regions in Fig. 2.4 (a)) and the  $\alpha$ -alumina matrix (expressed as bright regions in Fig. 2.4 (a)). The 2D porosities were 12.06 %, 13.80 %, and 1.80 % for 63 nm, 73 nm and 115 nm thickness nanoshells, respectively. Considering the shell thickness, we obtained from the 2D porosities the 3D porosities of each nanoshell structure. The obtained 3D porosities were 4.96 %, 5.28 %, and 4.99 % for a nanoshell thickness of 63, 73, and 115 nm, respectively.

From the cross-section TEM images in Fig. 2.4 (b), we obtained the size and position distribution of the nanopores (Fig. 2.4 (d)). The number of nanopores was quite large and followed a normal distribution. Fig. 2.4 (a) and (b) show that most nanopores have either spherical or spheroidal shapes; therefore, we assume that the radius measured from the cross-sectional TEM images provide statistically reasonable average values and a distribution similar to those obtained from top-view SEM images shown in Fig. 2.4 (c). For ellipsoids, we assumed that the nanopores are spherical, so that an FEM simulation could be efficiently performed. The radius of the ellipsoids was obtained by averaging the length of the semi-major and semi-minor axis of the ellipse. The average radius of the nanopores in each CSH nanoshell structure was found to be 11.48, 12.00, and 15.33 nm for the nanoshell thickness of 63,

73, and 115 nm, respectively, with normal distributions. Similar values of the radii and their distributions are shown in Fig. 2.4 (c). The average distance of the nanopore center from the free surface at which the tensile stress is developed was found to be 26.27, 30.25, and 42.70 nm for a nanoshell thickness of 63, 73, and 115 nm, respectively. The formation of the nanopores is attributed to the volume reduction of the alumina during the phase transformation from amorphous to  $\alpha$ -alumina [7, 8].

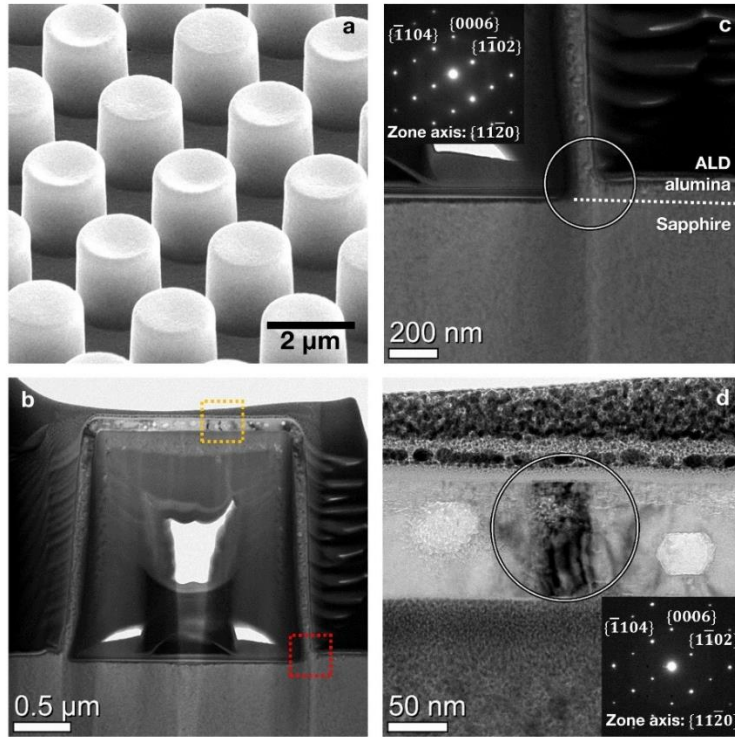


Figure 2.3 Cylinder-shaped  $\alpha$ -alumina hollow nanoshell structures. (a) Tilted-view SEM image of 73-nm thickness hollow nanoshell structure. (b) Cross-sectional TEM image of 73-nm thickness hollow nanoshell structure. (c, d) Magnified TEM images of area indicated with red and orange squares in b. Insets show SAED patterns of the area marked with white circles in each figure. (e) Distribution of radius of nanopores inside each nanoshell: 63-nm thickness nanoshell (top), 73-nm thickness nanoshell (middle), and 115-nm thickness nanoshell (bottom).

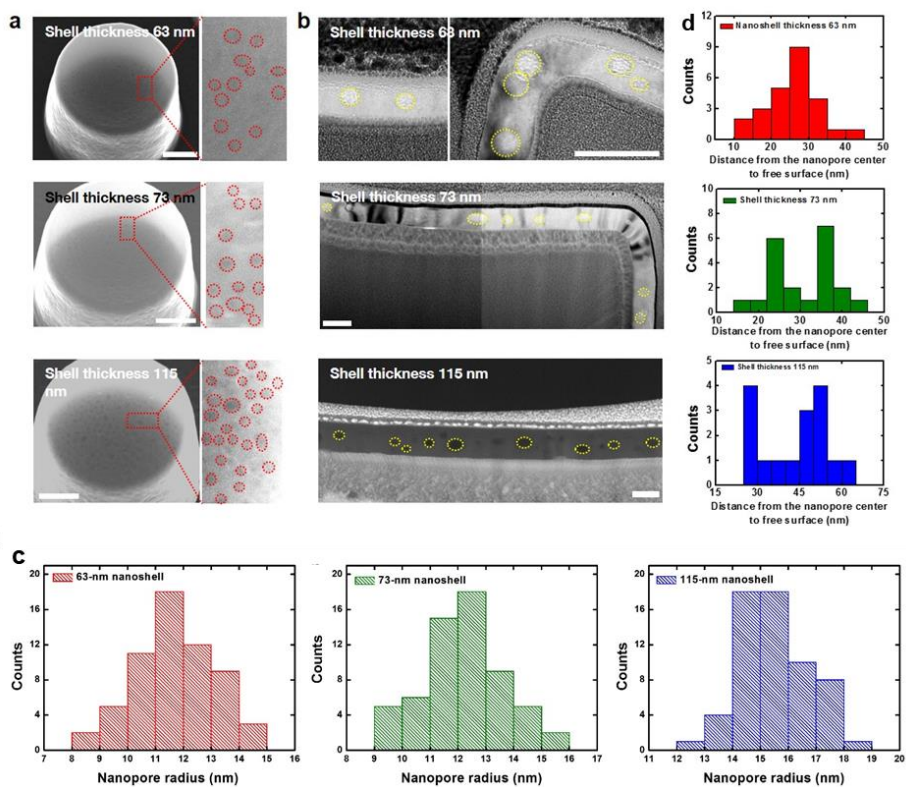


Figure 2.4 Analysis of the nanopore distributions in each nanoshell with thickness of 63 nm, 73 nm, and 115 nm. (a) Tilted-view SEM images (500 nm scale bars) and (b) cross-sectional TEM images (100 nm scale bars) of CSH nanoshell structures with thickness of 63, 73, and 115 nm, as indicated. The red and yellow circles indicate nanopores inside the nanoshells. (c) Radii distribution of the nanopores inside each nanoshell obtained from the SEM images. (d) Position distribution of the nanopores inside each nanoshell obtained from the TEM images.

## 2.3 Fracture strength of $\alpha$ -Alumina nanoshell structure

From the viewpoint of conventional fracture mechanics, the nanopores inside the nanoshell will act as critical stress concentration sites, while the fracture strength of the material is inversely proportional to the flaw size. The Griffith equation can provide us with a first-order approximation of the fracture strength ( $\sigma_F$ ) for flaw-containing brittle nanostructures. This is expressed as,

$$\sigma_F = \left( \frac{E\gamma_s}{(1-\nu^2)a} \right)^{1/2}, \quad (2.1)$$

where  $E$  is the elastic modulus,  $\gamma_s$  is the surface energy,  $\nu$  is the Poisson's ratio, and  $a$  is the flaw size. For  $\alpha$ -alumina,  $E$  is 425 GPa,  $\gamma_s$  is 4.83 J-m<sup>2</sup> for the (0001) surface, and  $\nu$  is 0.27 [9]. Assuming that the bulk  $\alpha$ -alumina incorporates a flaw of the same size as the critical nanopore initiating crack failure in this study, the fracture strength can be estimated to be about 13 GPa which is about four times greater than the fracture strength of bulk alumina with micropores. This prompts us to ask whether this high fracture strength, estimated from conventional fracture mechanics, is reasonable for nanoceramic materials with nanopores.



### 2.3.1 Experimental results

We conducted elaborate indentation tests with an in-situ nano-indentation system (Hysitron PI-85 SEM Picoindenter®) installed in a SEM (FEI Quanta FEG-250). Before indentation, a cono-spherical diamond indenter with a 1.1  $\mu\text{m}$  tip radius was carefully aligned to the center of each  $\alpha$ -alumina CSH nanoshell structure. The in-situ indentation tests were performed at a constant displacement rate at 10 nm/s. The thermal drift was calibrated by measuring the drift rate for 40 s before each indentation test. To investigate the fracture behavior of the nanoshell structures, the maximum indentation depth was set at a value greater than 100 nm. Fig. 2.5 presents a series of in-situ SEM images (Fig. 2.5 (a–e)) and the corresponding load–displacement curve (Fig. 2.5 (f)). Together, these describe the deformation and fracture behavior of the CSH nanoshell structure with a shell thickness of 73 nm for an indentation displacement of 300 nm. Most deformation and fracture occurs at the top surface of the CSH nanostructure (Fig. 2.5 (a–c)) until a catastrophic failure occurs (Fig. 2.5 (d)). The load–displacement curve (Fig. 2.5 (f)) indicates three notable pop-in discontinuities (denoted by the red, green, and blue dotted circles). The largest load drop at a displacement of 253 nm (blue dotted circle in Fig. 2.5 (f)) is associated with the catastrophic failure of the top surface (Fig. 2.5 (d)). Before the catastrophic failure, a small load drop near at the indenter displacement of 100 nm (red dotted circle in Fig. 2.5 (f)) and another pop-in discontinuity (green dotted circle in Fig. 2.5 (f)) are observed. A series of

additional indentation tests provided more detailed information for the critical stages which helped us to understand the overall deformation and failure process of the CSH nanoshell structure. As shown in the load–displacement in Fig. 2.5 (g), the indentation test with a displacement of 100 nm reveals that the unloading path is identical to the loading path. This indicates that the initial deformation before the first load drop is elastic without any structural failure at the top surface, as shown in Fig. 2.5 (b). Another indentation test explains that the first load drop was caused by radial crack initiation underneath the indenter tip. The top-view SEM image of the CSH nanoshell structure (Fig. 2.5 (h)), captured immediately after the first load drop, clearly shows newly generated radial cracks emanating from the center of the top surface of the structure. After radial crack initiation, the top surface of the CSH nanoshell structure was continuously deformed (Fig. 2.5 (c)) until the second pop-in occurs at around 190 nm. A SEM image (Fig. 2.5 (i)) of the top surface of the CSH nanoshell structure, captured immediately after the second pop-in event, shows circumferential crack formation in addition to radial crack propagation emanating from the center. Hence, the deformation behavior of the CSH nanoshell structure during the cono-spherical indentation can be summarized as initial elastic bending of the top surface followed by radial and circumferential crack formation at the center of the top surface before completely collapsing. (Fig. 2.6)

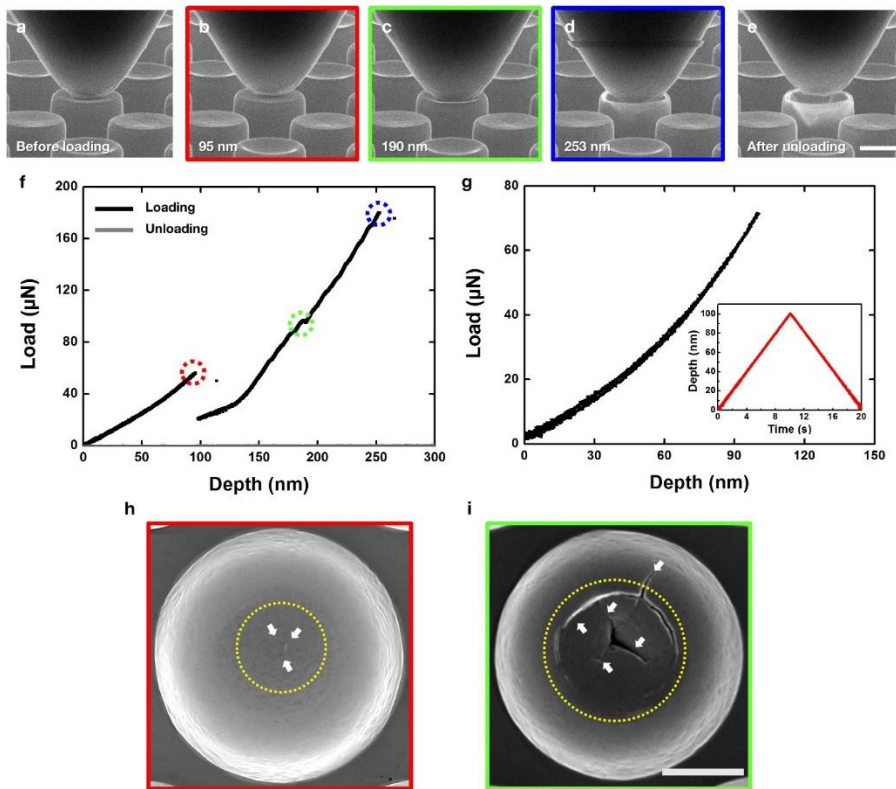


Figure 2.5 In-situ indentation test of 73-nm thickness CSH nanoshell structure. (a-e) Series of SEM images of in-situ indentation. (f) Load-displacement (L-D) curve of 300-nm indentation. (g) L-D curve of 100-nm indentation. Inset indicates load function. (h, i) Top-view SEM images of 73-nm thickness CSH nanoshell structure. The yellow circle and white arrows represent the contact area of the indenter tip and the deformation-induced cracks, respectively. SEM images with colored frames (b-d), (h-i) represent the tilted- and top-view SEM images of 73-nm thickness CSH nanoshell structures at each point marked with circles of the same color on the 300-nm indentation L-D curve (f). The scale bars are 1  $\mu\text{m}$ .

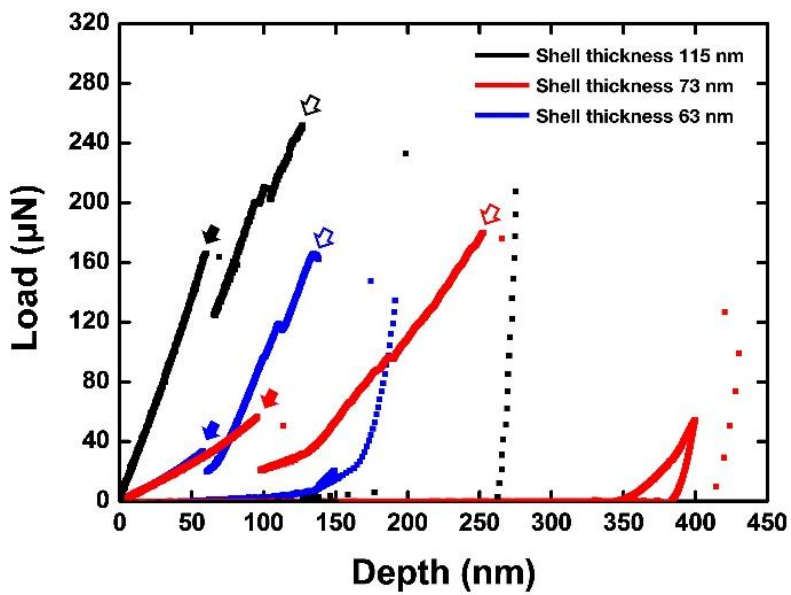


Figure 2.6 Load-displacement curves from in-situ indentation tests for each hollow nanoshell structure with shell thickness of 63 nm (blue), 73 nm (red), and 115 nm (black). The solid arrows and hollow arrows indicate crack initiation and structural collapse, respectively.

### 2.3.2 Computational results

Since the occurrence of a fracture relieves the elastically stored energy resulting from external loading, we can estimate the fracture strength of the  $\alpha$ -alumina in the CSH nanoshell structure by analyzing the stress evolution underneath the indenter at the first load drop which was caused by the initial radial crack formation. We estimated the fracture strength of the alumina nanoshell structures based on the experimental indentation data using a continuum-based simulation. Although we used nano-indentation testing to deform the nanostructure of the materials, the alumina nanoshell structure was a single crystalline solid with nanoscale voids. This suggests that grain boundary fractures, which are often a major fracture mechanism in nanocrystalline materials, do not need to be considered. Therefore, the deformation of the alumina nanoshell structures with nanopores was assumed to be linearly elastic before the fracture, because the ceramic fracture from the internal flaws relieves the elastically stored energy resulting from external loadings. The computational model was constructed using the ABAQUS Standard (Ver. 6.10) general finite element analysis software. As shown in Fig. 2.7, we established a 2D axisymmetric model based on the actual geometries of the nanoshell structures and applied 4-node bilinear axisymmetric quadrilateral elements (CAX4) with adaptive meshing to the model. The elastic modulus and Poisson's ratio of the sapphire wafer were set at 425 GPa and 0.27, respectively [9]. The nanopore-containing nanoshells were assumed to be solid

and the indenter was defined as a rigid body. Additionally, the elastic behavior was assumed to be isotropic. Zener's anisotropy factor ( $A$ ) is used to specify elastic anisotropy in cubic and hexagonal materials and expressed as follow

$$A = 2(S_{11} - S_{12})/S_{44} = 2 C_{44}/(C_{11} - C_{12}) \quad (2.2)$$

where  $S_{11}$ ,  $S_{12}$ ,  $S_{44}$  are the compliance constants and  $C_{11}$ ,  $C_{12}$ ,  $C_{44}$  are the stiffness constants of the materials [10]. When the factor is unity, the elastic properties are isotropic, but it can deviate from isotropy by the factor being either greater than or less than unity. Zener's anisotropy factor of the  $\alpha$ -alumina is 0.91 which is close to the unity [11, 12]. Based on this, we confirmed that the computational model considering the anisotropy of the material exhibits similar elastic behavior with the isotropic model (Fig. 2.8). To investigate the influence of the nanopores on the elastic modulus, we extracted the effective elastic modulus by matching the experimental and computational load-displacement curves. By iteratively optimizing the elastic modulus of the CSH nanoshell structures in the computational model, we found that the load-displacement curves of the computational analysis were in good agreement with those of the experimental results when the elastic moduli inputs were optimized to 360 GPa, 370 GPa, and 350 GPa for the 63-, 73-, and 115-nm thicknesses of the  $\alpha$ -alumina CSH nanoshell structures, respectively.

Pabst *et al.* suggested that the effective elastic modulus of porous ceramics is inversely proportional to the porosity and can be expressed as,

$$\frac{E_{effective}}{E_{intrinsic}} = (1 - \phi) \left(1 - \frac{\phi}{\phi_c}\right), \quad (2.3)$$

where  $E_{intrinsic}$  is the intrinsic elastic modulus,  $\phi$  is the porosity and  $\phi_c$  is the critical porosity at which a porous ceramic loses its integrity and collapses [13]. By substituting the porosity of the  $\alpha$ -alumina nanoshell structures (0.05), as obtained by SEM analysis, and the parameter for the critical porosity (0.684) into Equation (2), the effective elastic modulus is found to be about 360 GPa which is 14 % smaller than the intrinsic elastic modulus of the  $\alpha$ -alumina phase (425 GPa). This is consistent with the extracted elastic modulus values from the experimental and computational results which confirms that the nanopores formed inside the nanoshells significantly affect the elastic deformation behavior of the  $\alpha$ -alumina CSH nanostructures. Hence, we used these effective modulus values as our computational inputs to reflect the effect of the nanopores during elastic deformation. We then evaluated the failure stress developed underneath the indenter before the first load drop occurs as a result of radial crack formation (Fig. 2.9).

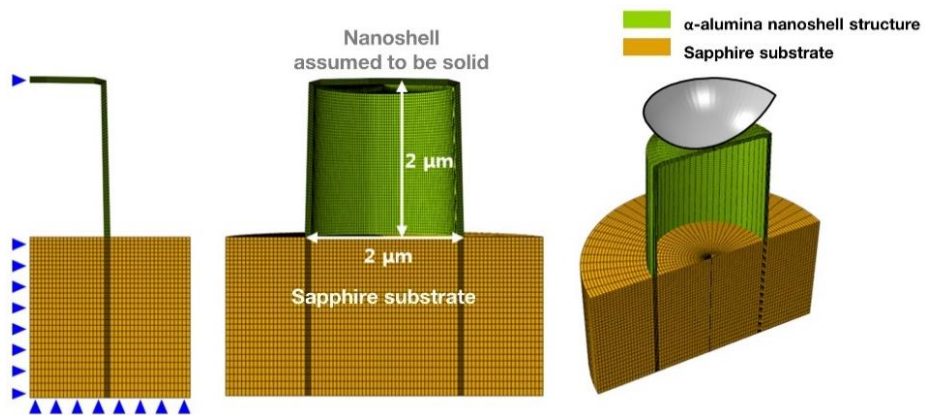


Figure 2.7 Representation of the computational model for in-situ indentation tests. The light green, orange, and gray sections indicate the  $\alpha$ -alumina hollow nanoshell structures, sapphire substrate, and cono-spherical indenter, respectively. The blue triangles indicate the boundary conditions.



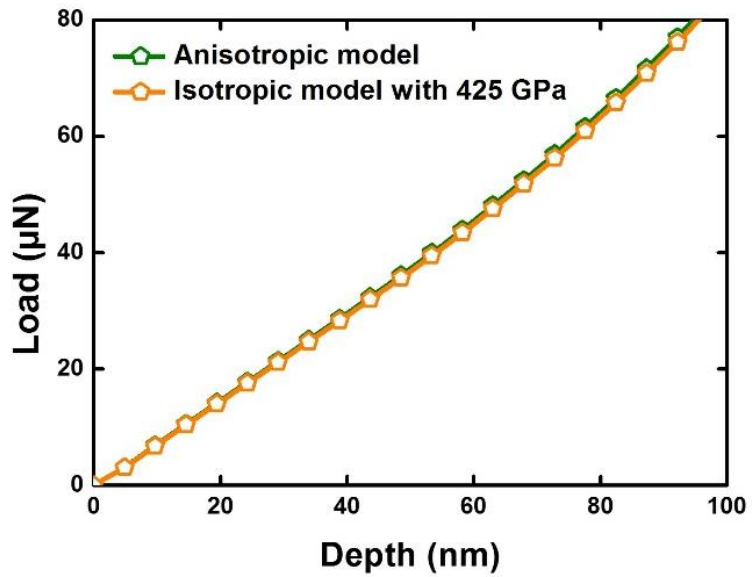


Figure 2.8 Load-displacement curves of the finite element simulations using an anisotropic model with elastic constants for the alpha alumina (green) and an isotropic model with elastic modulus of 425 GPa (orange).

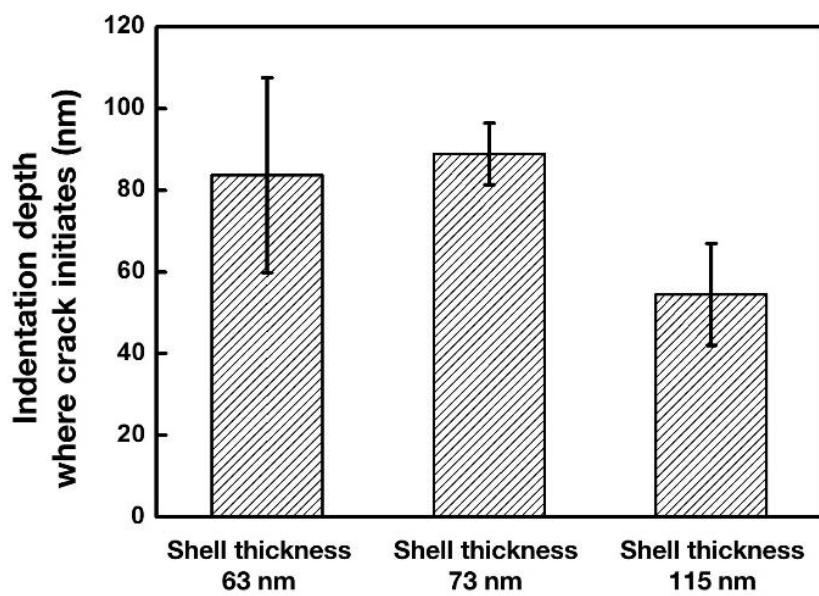


Figure 2.9 Average indentation depth where crack initiates for each hollow nanoshell structure with shell thickness of 63, 73, and 115 nm, as indicated.

### 2.3.3 Fracture strength and fracture criteria of the $\alpha$ -alumina nanoshell structure

As shown in Fig. 2.10, the tensile stresses were developed at the lower part of the top surface area of the CSH nanoshell structure. When the indentation depth is reached before the first load drops in Fig. 2.10 (a-c), we found that the maximum principal tensile stresses reach 15.29 ( $\pm 1.89$ ), 16.65 ( $\pm 0.72$ ), and 18.05 ( $\pm 0.83$ ) GPa (standard deviation in parentheses) for the CSH nanoshell structures with shell thickness of 63, 73, and 115 nm, respectively (Fig. 2.10 (d)). If we choose to use the maximum principal stress theory as our fracture criterion among the different failure criteria, the above maximum principal tensile strength values become the fracture strengths of the  $\alpha$ -alumina CSH structures, which are an order of magnitude higher than that of the microscale  $\alpha$ -alumina, for which the values are in the order of a few gigapascals [14, 15].

When the external load reaches the fracture strength, the maximum principal stress around the critical flaw initiating failure should exceed the theoretical strength. To confirm that our nano ceramic structures with nanopores also conform to the same failure mechanism, we constructed a model CSH nanoshell structure including the critical nanopore located at the bottom-center of the top surface area, as shown in Figure 2.11. The critical nanopore was assumed a sphere and was located at the center of the CSH nanoshell structure's top surface. The exact position and size of the critical nanopores were defined by considering the stress concentration factor.

The crack was generated near the nanopores with the highest stress

concentration factor. The stress concentration factor depends on the size and position of the nanopore. Based on the nanopore information obtained from SEM and TEM analysis, we calculated the stress concentration factors of the nanopores in each nanoshell. Considering axial symmetry, we applied the stress concentration factor from bending a circular hole-containing beam to our model. The stress concentration factor  $k$ , is expressed as follows [16, 17]:

$$\sigma_{with\ hole} = k\sigma_{without\ hole},$$

$$k = K_1 + K_2 \left(\frac{2c}{t}\right) + K_3 \left(\frac{2c}{t}\right)^2 + K_4 \left(\frac{2c}{t}\right)^3,$$

$$K_1 = 3.022 - 0.422\frac{r}{c} + 3.556\left(\frac{r}{c}\right)^2,$$

$$K_2 = -0.569 + 2.664\frac{r}{c} - 4.397\left(\frac{r}{c}\right)^2,$$

$$K_3 = 3.138 - 18.367\frac{r}{c} + 28.093\left(\frac{r}{c}\right)^2,$$

$$K_4 = -3.519 + 16.125\frac{r}{c} - 27.252\left(\frac{r}{c}\right)^2$$

where  $t$  is the beam thickness,  $r$  is the radius of the hole, and  $c$  is the distance of the center of a hole from to the surface that the tensile stress is applied. Four nanopores with the highest stress concentration factor were chosen from more than 10 nanopores in each nanoshell. The parameters for the critical nanopores were set by averaging the size and position of the chosen nanopores (Table 2.1). The stress distribution near the critical nanopores, at which crack initiation occurred, was obtained by moving the indenter tip to the

depth where the first load drop in the load-displacement curve was observed.

Fig. 2.10 (e) shows the maximum principal stress distribution around the critical nanopore in the CSH nanoshell structures with thicknesses of 63, 73, and 115 nm. The highly concentrated maximum tensile principal stresses were developed at the bottom of the critical nanopores. Their values were 32.30 ( $\pm 4.72$ ), 31.05 ( $\pm 1.40$ ), and 34.89 ( $\pm 1.77$ ) GPa, respectively. In general, the theoretical tensile strength of a perfect ceramic is about  $E/10$ , while that of  $\alpha$ -alumina is between 31 GPa and 38 GPa [15, 18]. Therefore, we confirmed that the fracture of the alumina in the CSH nanoshell structures occurs when the maximum principal tensile stress reaches the theoretical strength at the critical nanopore before the first pop-in. Note that, even with this critical nanopore in the model structure, the overall stress distribution and values around the bottom part of the top surface area are identical to those of the elastic continuum models with the effective modulus shown in Fig. 2.10 (d). Hence, the fracture strength of the  $\alpha$ -alumina in the CSH nanoshell structure containing multiple nanopores is estimated to be around 16 GPa. Interestingly, this remarkably high fracture strength is also in good agreement with the first-order approximation obtained with the Griffith equation (around 13 GPa) with the flaw size of the critical nanopore, implying that the value of the high fracture strength as estimated using conventional fracture mechanics, is reasonable for nanoceramic materials containing nanopores. In addition, the size effect phenomenon of “smaller is stronger” in ceramic materials at the nanoscale level can also be explained not

by the shell thickness but by the size of the flaws, implying that the fracture strength increases drastically because the size of the nanopores decreases to the nanoscale regime as the size of the specimen reaches the nanoscale level. Therefore, it is possible to easily obtain a fracture strength at the gigapascal scale. Furthermore, unlike bulk ceramic materials, the ceramic nanostructures exhibit a narrower distribution of flaw sizes and shapes because of the effect of an upper bound, such as the nanoshell thickness in the present study. This implies that the fracture strength can be more accurately predicted for a ceramic nanostructure than for a bulk ceramic. When the ceramic nanostructure is utilized as a structural material, it is possible not only to secure an ultrahigh fracture strength, but also to precisely predict the fracture strength, so that the mechanical reliability can be greatly improved.

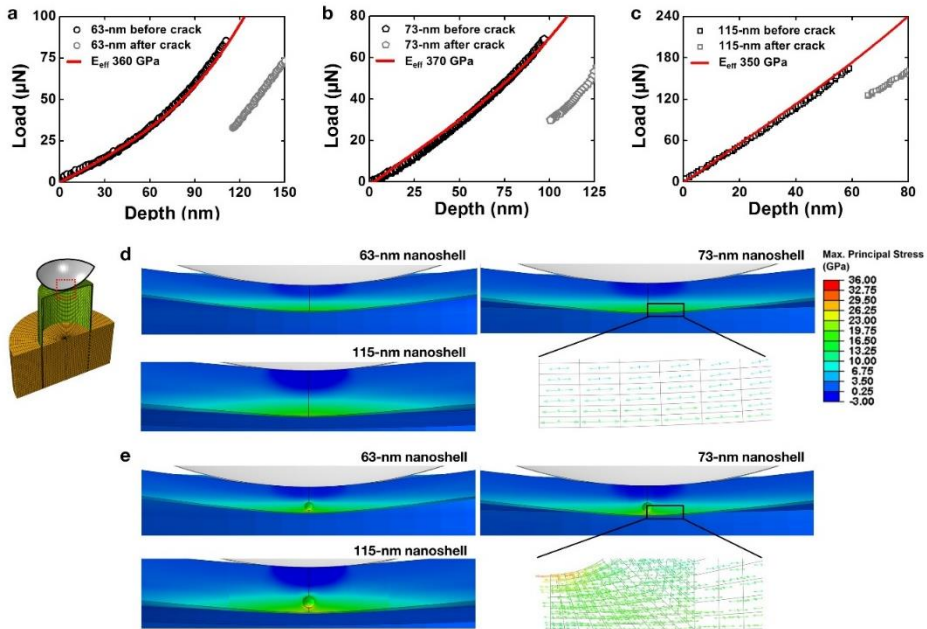


Figure 2.10 Finite element analysis of in-situ indentation tests for CSH nanoshell structures. (a-c) Representative experimental L-D curves of 63-nm thickness (a), 73-nm thickness (b), and 115-nm thickness (c) CSH nanoshell structures and corresponding FE simulations (red line). The black and gray points represent the material response before and after the crack initiation, respectively. (d-left) Cut-view of meshes used in FE simulation. The green, orange, and gray elements indicate the  $\alpha$ -alumina hollow nanoshell structures, sapphire substrate, and indenter tip, respectively. (d-right) Maximum principal stress distribution within each CSH nanoshell structure. The nanoshell is assumed to be solid. (e) Maximum principal stress distribution around critical nanopore for each CSH nanoshell structure.

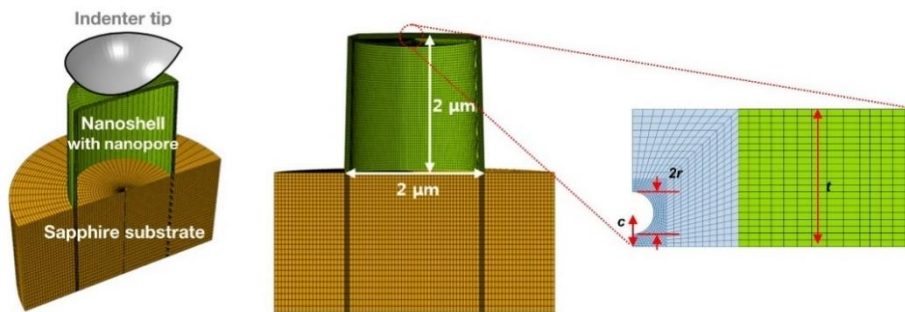


Figure 2.11 Representation of the computational model for evaluating stress evolution near the nanopores. The light-blue section represents the stress concentration part that contains the critical nanopore and  $\alpha$ -alumina matrix, and the green sections represent the other  $\alpha$ -alumina matrix, which is assumed a solid with an effective elastic modulus.



Table 2.1 Radius and position of the chosen-nanopores and the critical nanopore.

<b>Nanoshell thickness</b>		<b>#1</b>	<b>#2</b>	<b>#3</b>	<b>#4</b>	<b>Average</b>
<b>63 nm thickness</b>	Radius [nm]	13.45	10.11	8.06	9.12	10.18
	Distance [nm]	32.73	28.54	22.23	22.45	26.48
<b>73 nm thickness</b>	Radius [nm]	13.35	11.12	12.23	11.70	12.10
	Distance [nm]	37.83	34.46	32.24	27.18	32.93
<b>115 nm thickness</b>	Radius [nm]	16.19	18.38	15.81	12.89	15.81
	Distance [nm]	41.42	49.25	41.44	40.01	43.03

## 2.4 Applicability of 3D ceramic nanostructure

We will demonstrate how this ultra-strong nanoceramic can be utilized in an actual GaN LED application. Up to this point, we have used a CSH nanoshell structure as our model hollow nanoshell structure to determine the mechanical properties of  $\alpha$ -alumina with nanopores at the nanoscale. However, we chose a hemisphere-shaped hollow nanoshell structure (henceforth referred to as the HSH nanoshell structure) for an actual GaN LED application. We selected this structure because, according to the results of previous studies, it offers a better light-extraction efficiency and output power than the CSH nanoshell [6]. A new GaN LED design with an HSH nanoshell structure is expected to resolve the following key mechanical issues: (a) whether the newly incorporated alumina nanoshell structures can effectively generate a stress gradient in the GaN film, allowing us to reduce the number of threading dislocations and defect sites and thus mitigate the residual stress in the thin film to prevent serious wafer bowing and (b) whether the nanoshell structures are strong enough to survive under the thermal stress produced by the conventional GaN LED fabrication process.

#### 2.4.1 Mechanical reliability of the nanoshell structure

To address the above mechanical issues before the actual fabrication stage, we constructed computational models of the GaN LEDs with and without the HSH nanostructures. Unit cell models of dimensions  $1.5 \times 1.5 \times 10.2 \mu\text{m}^3$  were established for the conventional GaN LEDs and  $\alpha$ -alumina hollow nanoshell structure-incorporated GaN LEDs based on the actual geometry (Fig. 2.12, 2.13 (a)). The unit cell models for the nanoshell structure-incorporated GaN LEDs included a GaN thin film of  $3.2 \mu\text{m}$  thickness, the  $\alpha$ -alumina hollow nanoshell structures, and a sapphire substrate of  $7.0 \mu\text{m}$  thickness. The hemispherical hollow nanoshell structure, which was chosen as the model structure, was located between the GaN thin film and sapphire substrate. Periodic boundary conditions along the in-plane axes were adopted [19-22]. The thermal expansion coefficients were  $7.5 \times 10^{-6} / \text{K}$  and  $5.59 \times 10^{-6} / \text{K}$  for the sapphire substrate and GaN thin film, respectively [4]. The thermal expansion coefficient for the  $\alpha$ -alumina nanoshell structures was assumed to be identical to that of the sapphire substrate. The fabrication of a GaN LED typically starts with the deposition of a GaN thin film on a sapphire wafer at a temperature of  $1040 \text{ }^\circ\text{C}$ , after which it is cooled to room temperature. This is reflected in the simulations. As shown in Fig. 2.13 (b), a residual compressive stress of about 800 MPa was homogeneously distributed in the conventional GaN LED model after the cooling process. On the other hand, in the GaN film with the HSH nanoshell structure, stress gradients are generated around its periphery and significantly

reduce the residual stress. This reduction in the residual compressive stress in the GaN thin film is significant enough to alleviate wafer bowing in a conventional GaN LED [4]. In addition, the shape and amount of the stress gradient field formed around the nanoshells is similar to those reported previously, which is required to reduce the density of the threading dislocations in the GaN thin film [4]. Fig. 2.13 (c) presents the maximum principal stress distribution within the HSH nanoshell structure after the cooling process, which was induced by the residual compressive stress in the GaN thin film. While a small compressive stress was observed in the top surface of the hollow nanoshell structure, a high tensile stress of 1.4 GPa along the y-axis was developed in the circumferential part of the structure. However, because the  $\alpha$ -alumina nanoshell structure has an ultrahigh fracture strength of around 16 GPa with a factor of safety of about 10, the  $\alpha$ -alumina HSH nanoshell structures will not fracture through the conventional GaN LED fabrication process.

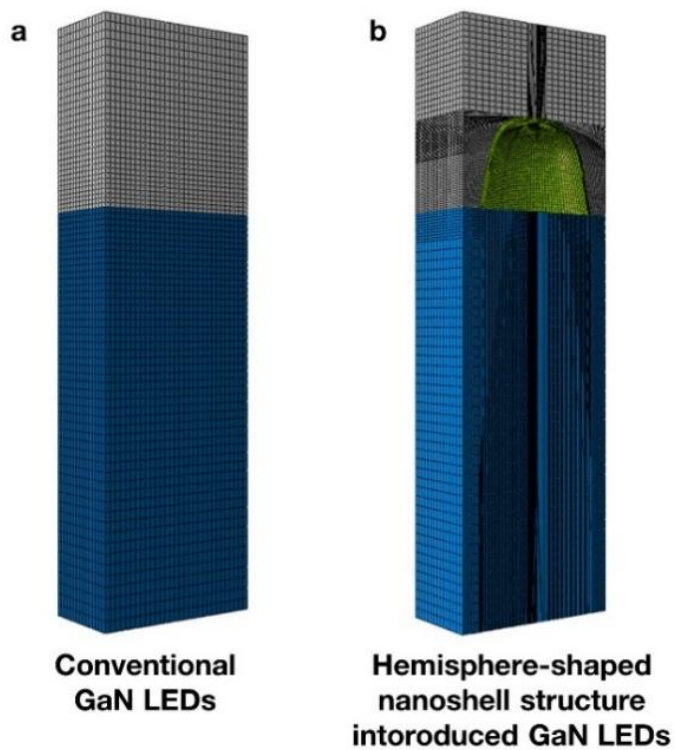


Figure 2.12 Representation of the computational model of (a) conventional GaN LEDs and (b)  $\alpha$ -alumina hemispherical hollow nanoshell structure-incorporated GaN LEDs. The gray, green, and dark-blue areas indicate the GaN thin film, hollow nanoshell structures, and sapphire substrate, respectively.

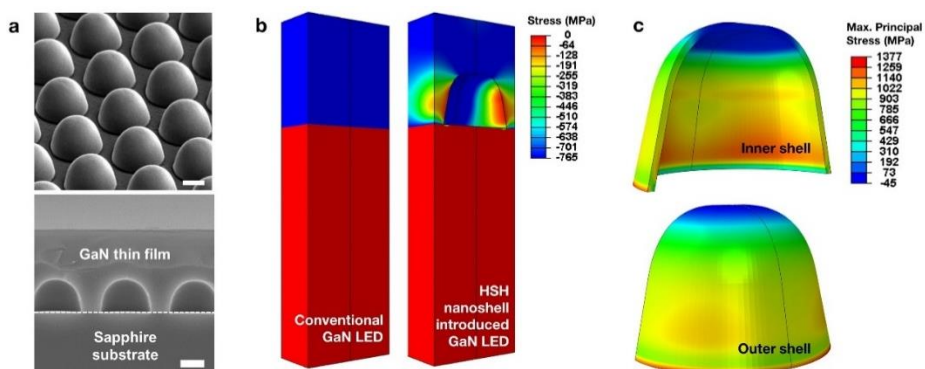


Figure 2.13 Introduction of hemisphere-shaped  $\alpha$ -alumina hollow nanoshell structures to GaN LEDs. (a) Tilted-view SEM image of HSH nanoshell structure (top) and cross-sectional SEM image of HSH nanoshell structure (bottom) after GaN thin film deposition. Scale bar is 1  $\mu\text{m}$ . (b) Residual stress distribution within GaN thin film and sapphire substrate of conventional (left) and HSH nanoshell structure-incorporated (right) GaN LEDs when cooling from 1040  $^{\circ}\text{C}$  to 25  $^{\circ}\text{C}$  ends. (c) Maximum principal stress evolution of inner nanoshell structure (top) and outer nanoshell structure (bottom) when cooling from 1040  $^{\circ}\text{C}$  to 25  $^{\circ}\text{C}$  ends.

#### 2.4.2 GaN LEDs incorporated with the nanoshell structures

Since the suggested design of the  $\alpha$ -alumina HSH nanoshell structures in the GaN LEDs is mechanically reliable, we finally fabricated actual GaN LEDs with  $\alpha$ -alumina HSH nanoshell structures. An LED structure was grown on two-inch sapphire substrates with and without HSH nanoshell structures in the same batch using metal organic chemical vapor deposition. For the LED structure, a 3  $\mu\text{m}$  thick un-doped GaN layer was grown on the substrates, followed by the growth of a 2.5  $\mu\text{m}$  thick n-type GaN, 5 periods of InGaN (3 nm)/GaN (7 nm) multiple quantum well, and p-type GaN (150 nm). Trimethylgallium, trimethylindium, and  $\text{NH}_3$  were used as precursors for Ga, In, and N, respectively. For the n- and p-type GaN layers, silane and bis-cyclopentadienyl magnesium were used as the source of dopants, respectively. Afterwards, mesa etching of  $1000 \times 1000 \mu\text{m}^2$  was performed using inductively coupled plasma processing to fabricate the LED chips. An ITO (200 nm) transparent conductive layer and an Au (500 nm)/Ni (25 nm)/Cr (20 nm) electrode were deposited. Light output powers of the LED chips with and without HSH nanoshell structures were measured on-wafer using an EtaMax LIF-AT system and an Ocean Optics FOIS-1 integrating sphere [5]. As shown in Fig. 2.14, GaN LEDs with the  $\alpha$ -alumina HSH nanostructure provide a significantly improved light-extraction efficiency with an improved output power that is 2.2 times higher than that of conventional GaN LEDs.

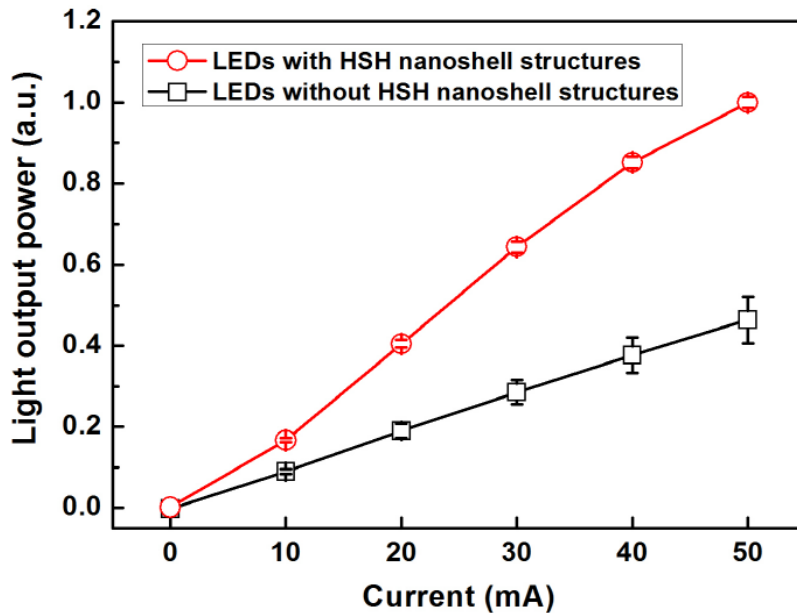
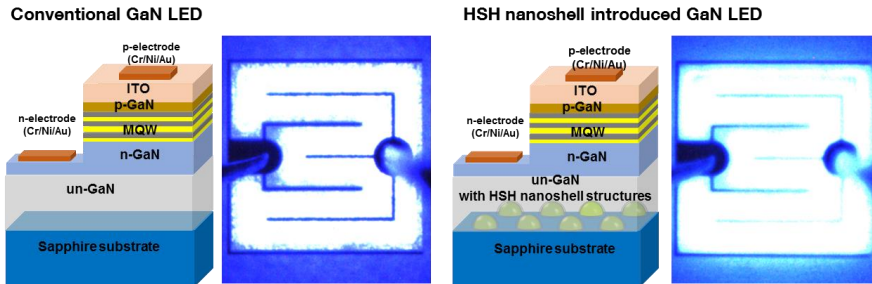


Figure 2.14 Schematic diagrams and turn-on images of conventional (left) and HSH nanoshell structures-incorporated (right) GaN LEDs with average light output power of the LED chips with HSH nanoshell structures (red spheres) and without HSH nanoshell structures (black squares).



## 2.5 Conclusion

In this chapter, we demonstrated that the  $\alpha$ -alumina hollow nanoshell structure can exhibit an ultrahigh fracture strength even though it contains a significant number of nanopores. Our experimental and computational analyses revealed that the ultrahigh fracture strength of the  $\alpha$ -alumina hollow nanoshell structure can be explained from the perspective of conventional fracture mechanics, in that the fracture strength drastically increases because the size of the flaws decreases to the nano-scale regime. Furthermore, we could state with confidence that the hollow nanoshell structure successfully maintains its shape as an interlayer even after the fabrication process has ended, as predicted by the computational analysis, and thus improves the light-extraction efficiency and output power of a GaN LED. We believe that the fundamental understanding of the size effect of fracture strength gained through this study will provide an invaluable baseline for the design of 3D nanostructures in advanced devices.

## 2.6 References

- [1] A. Dadgar, F. Schulze, T. Zettler, K. Haberland, R. Clos, G. Straßburger, J. Bläsing, A. Diez, A. Krost, *Journal of Crystal Growth*, 272 (2004) 72-75.
- [2] A. Hangleiter, C. Netzel, D. Fuhrmann, F. Hitzel, L. Hoffmann, H. Bremers, U. Rossow, G. Ade, P. Hinze, *Philosophical Magazine*, 87 (2007) 2041-2065.
- [3] G.B. Stringfellow, *Journal of Crystal Growth*, 312 (2010) 735-749.
- [4] J. Kim, H. Woo, K. Joo, S. Tae, J. Park, D. Moon, S.H. Park, J. Jang, Y. Cho, J. Park, H. Yuh, G.D. Lee, I.S. Choi, Y. Nanishi, H.N. Han, K. Char, E. Yoon, *Sci Rep*, 3 (2013) 3201.
- [5] J. Jang, D. Moon, H.-J. Lee, D. Lee, D. Choi, D. Bae, H. Yuh, Y. Moon, Y. Park, E. Yoon, *Journal of Crystal Growth*, 430 (2015) 41-45.
- [6] Y.J. Moon, D. Moon, J. Jang, J.Y. Na, J.H. Song, M.K. Seo, S. Kim, D. Bae, E.H. Park, Y. Park, S.K. Kim, E. Yoon, *Nano Lett*, 16 (2016) 3301-3308.
- [7] D.R. Clarke, *phys. stat. sol. (a)*, 166 (1998) 183-196.
- [8] M. Vahtrus, M. Umallas, B. Polyakov, L. Dorogin, R. Saar, M. Tamme, K. Saal, R. Löhmus, S. Vlassov, *Materials Characterization*, 107 (2015) 119-124.
- [9] E.R. Dobrovinskaya, L.A. Lytvynov, V. Pishchik, *Sapphire: Material, Manufacturing, Applications*, Springer (2009).
- [10] D.N. Lee, *Texture and Related Phenomena*, The Korean Institute of Metals

- and Materials* (2006).
- [11] E.S. Zouboulis, M. Grimsditch, *Journal of Applied Physics*, 70 (1991) 772-776.
- [12] J.M. Winey, Y.M. Gupta, D.E. Hare, *Journal of Applied Physics*, 90 (2001) 3109-3111.
- [13] W. Pabst, E. Gregorová, G. Tichá, *Journal of the European Ceramic Society*, 26 (2006) 1085-1097.
- [14] P.D. Bayer, R.E. Cooper, *Journal of Materials Science*, 2 (1967) 233-237.
- [15] R.J. Brook, *Concise encyclopedia of advanced ceramic materials*, Pergamon press (1991).
- [16] R.J. Roark, *Roark's formulas for stress and strain*, 7th ed., McGraw-Hill (2002).
- [17] S.I. Cha, K.H. Lee, H.J. Ryu, S.H. Hong, *Materials Science and Engineering A*, 486 (2008) 404-408.
- [18] C.B. Carter, M.G. Norton, *Ceramic Materials: Science and Engineering*, 2nd ed., Springer (2013).
- [19] B.J. Kim, Y. Cho, M.S. Jung, H.A. Shin, M.W. Moon, H.N. Han, K.T. Nam, Y.C. Joo, I.S. Choi, *Small*, 8 (2012) 3300-3306.
- [20] Y. Cho, T.-H. Ahn, H.-H. Cho, J.-H. Shin, J.H. Moon, S. Yang, I.S. Choi, H.N. Han, J. Li, *Modelling and Simulation in Materials Science and Engineering*, 21 (2013).
- [21] A. Yoon, J.Y. Park, J.M. Jeon, Y. Cho, J.B. Park, G.C. Yi, K.H. Oh, H.N.

Han, M. Kim, *Small*, 9 (2013) 2255-2259.

[22] H.-H. Cho, Y. Cho, H.N. Han, *Acta Materialia*, 97 (2015) 199-206.

## **Chapter 3**

# Ductile deformation behavior of ceramics in nanoscale induced by electron-beam irradiation

### **3.1 Introduction**

Plasticity of material has a direct correlation to formability. Ceramics, which are the most widely known low-plasticity material, only exhibit the brittle fracture when subjected to stress, unless placed at a high temperature condition. In order to fabricate a ceramic-based structural material, complex processes must be involved: High temperature heating or sintering for a bulk scale, deposition methods for micro/nano scales. Especially for nanoceramics, simple geometries, such as wires, films, and spheres, are only valid to fabrication. Despite the exceptional mechanical properties of the 3D nanoceramic with complex geometries and their novel applications from a damage tolerance material to advanced electronics reported recently, low plasticity limits their potential for wider application [1-4].

Recent researches have made a breakthrough in the plasticity of ceramics by utilizing an electron-beam (henceforth, referred to as “E-beam”) irradiation. Amorphous silica spheres of submicron size exhibit mechanical softening and substantial permanent deformation when uniaxially compressed under the E-

beam irradiation in a transmission electron microscopy (TEM) [5-7]. However, since most researches have focused on the E-beam effects on deformation behaviors of amorphous silica, only a few results for other ceramics have been reported [8, 9]. In addition, the majority of studies have investigated the E-beam induced deformation behaviors of amorphous silica within the TEM [5-7, 10, 11]. TEM not only generates a fixed high energy E-beam of several hundred keV, but also only allows very simple mechanical tests, such as tensile test of a nanowire and compression test of a particle, owing to its limited chamber size. Despite the in-situ TEM system provides a real-time microstructural changes of the material during the E-beam irradiation, but not sufficient to rigorously investigate the E-beam induced deformation behaviors under the various beam conditions and to confirm the improved formability of the material in various ways.

Fundamental questions about the E-beam induced deformation behaviors are still unresolved. How do the E-beam induced deformation behaviors of the amorphous silica change when we change the E-beam conditions? More specifically, can we observe the E-beam induced deformation behaviors even under the low energy E-beam? What is the most important factor in determining the E-beam induced deformation behaviors of the amorphous silica? Can we observe the E-beam induced deformation behaviors from other ceramic materials? And most of all, by simply irradiating the E-beam, can we freely deform the material into the certain shapes?

In this paper, we utilize an in-situ scanning electron microscopy (SEM) compression system to explore the E-beam induced deformation behaviors of the ceramic materials. The beauty of SEM is that we can easily utilize the low energy E-beam with various conditions by regulating the acceleration voltage and the beam current in each pixel. With the E-beam of the SEM, we rigorously investigated the low energy E-beam induced mechanical softening and permanent deformation of the amorphous silica and their relationship with the beam parameters, such as the acceleration voltage, the beam current, etc. Experiments and simulations have shown that the interacting volume between the material and the incident electrons is an important factor for the E-beam induced deformation behavior. Moreover, we expand the concept of the E-beam induced deformation behavior to various ceramics, including amorphous and crystalline ceramics, by performing the similar in-situ compression tests under the E-beam of SEM. Surprising findings on the E-beam induced deformation behaviors of the nanoceramics enable us to perform a glasswork, normally conducted at high temperature above a glass transition temperature for the bulk scale, inside the SEM by irradiating the materials with the E-beam. We have successfully demonstrated the feasibility of “Nano-glasswork” by deforming the amorphous silica nanoshell spheres in various ways. We believe that our research can provide a specific E-beam condition for triggering substantial plastic deformation of the low plasticity ceramics and also pioneer new fields in the fabrication processes of the nanoceramic structural materials.

## 3.2 Materials and methods

### 3.2.1 Specimen preparation

We fabricated amorphous silica spheres through a sol-gel method, the Stöber process. Molecular precursor tetraethylorthosilicate (TEOS) is mixed with ammonium hydroxide as a catalyst [12]. Through hydrolysis and polycondensation process, submicron sized silica solid spheres with diameter of 290 nm are synthesized (Fig. 3.1) and dispersed in the solution. Transferring the amorphous silica spheres to the sapphire substrate was conducted through spin coating [13]. In order to remove the residues in the amorphous silica sphere, such as physically absorbed water, residual solvent, and pyrolysis of CH<sub>3</sub>, and fix them on the sapphire substrate, we conducted heat treatment at 900 °C for 6 hours in the argon atmosphere [14, 15].

Amorphous silica nanoshell spheres with shell thickness of 20 nm can be fabricated by synthesizing the amorphous silica thin film on polystyrene (PS) spheres [13]. During the Stöber process, we added the 250 nm diameter PS spheres with the TEOS and the ammonium hydroxide and synthesized PS/amorphous silica core-shell spheres. Through spin coating, the PS/amorphous silica core-shell spheres were dispersed on the sapphire substrate. The amorphous silica nanoshell spheres were successfully obtained by the same heat treatment above. During the heat treatment, PS core also evaporated with the residues.



Amorphous and crystalline ceramic ( $\text{SiO}_2$ ,  $\text{Al}_2\text{O}_3$ ,  $\text{TiO}_2$ ,  $\text{ZnO}$ ) pillars with diameter of 280 nm and height of 900 nm were fabricated by focused ion-beam (FIB) milling on each substrates. Each amorphous ceramic substrates were fabricated by the hydrothermal ( $\text{SiO}_2$ ) and the E-beam evaporation method ( $\text{Al}_2\text{O}_3$  and  $\text{TiO}_2$ ). Crystalline ceramic substrates were fabricated by the hydrothermal ( $\text{SiO}_2$  and  $\text{ZnO}$ ), the Kyropoulos method ( $\text{Al}_2\text{O}_3$ ), and the floating zone method ( $\text{TiO}_2$ ). Ion-beam with 30 kV acceleration voltage was used to roughly mill (3 nA) and finely mill (10 pA) the substrate in order to fabricate the pillars.

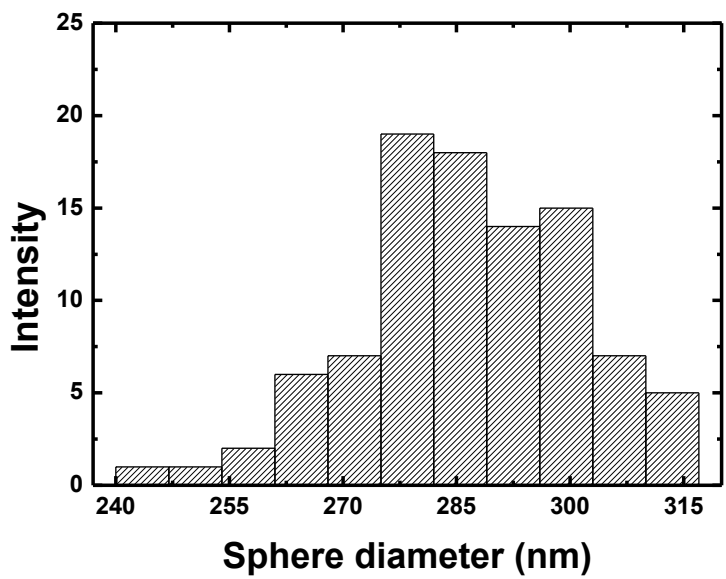


Figure 3.1 Diameter distribution of the amorphous silica spheres.

### 3.2.2 Experimental methods

Elaborate compression tests with an in-situ nano-indentation system (Hysitron PI-85 SEM Picoindenter®) installed in a SEM (FEI Quanta FEG-250 and FEI Nova 600 NanoLab). Cono-spherical diamond indenter with a 500 nm tip radius and flat punch diamond indenter were used to conduct the compression test on the solid/nanoshell spheres and pillars, respectively. For the solid/nanoshell spheres, in-situ compression tests were performed at a constant loading rate of  $0.4 \mu\text{N/s}$  up to maximum load of  $100 \mu\text{N}$ . In case of the pillars, tests were performed at a constant strain rate of  $0.00006/\text{s}$  up to maximum strain of 0.15. The thermal drift was compensated by measuring the drift rate for 40 s before each indentation test. We conducted in-situ compression tests under various E-beam conditions. Details on the E-beam conditions can be found in Table 3.1.

Table 3.1 E-beam conditions for in-situ compression tests.

	<b>Solid/Nanoshell spheres</b>	<b>Pillars</b>
<b>Acceleration voltage (kV)</b>	1, 2, 3, 5, 10, 20, 25, 30	5, 10
<b>Beam current (pA)</b>	3.1, 13, 50, 100, 200	25, 98, 400, 1600, 6300
<b>Magnification</b>	100,000	100,000
<b>Scan rate</b>	1 $\mu$ sec	100 nsec
<b>Number of pixels</b>	1024 $\times$ 884	512 $\times$ 442

### **3.3 Electron-beam effect on deformation behavior of amorphous ceramics**

#### **3.3.1 E-beam effect on deformation behavior of amorphous silica**

In order to investigate the irradiation effect of the low energy E-beam with few keV acceleration voltages on the deformation behavior of the amorphous silica spheres, we performed the in-situ SEM compression test with fixed maximum load under various E-beam conditions. The presence of the E-beam irradiation effects was confirmed based on the materials' response during the compression test and the SEM images of compressed spheres. First, for the sphere compressed without the E-beam irradiation, most deformation occur in the upper part of the sphere which was in contact with the indenter, and so was the compressed sphere under the E-beam with 1kV acceleration voltage. Under the other beam conditions, however, the deformation occurred in the entire sphere. Moreover, under certain conditions, the spheres expanded in the transverse direction of the loading direction and changed into a pancake-like shape (Fig. 3.2).

The SEM images of the compressed spheres provide useful information for deducing the deformation mechanism. Owing to strong covalent bonds between the Si and O atoms, silica requires high energy to break the interatomic bond and plastically deform. For this reason, only the plasticity induced by densifying an empty space of about 20% of the total volume rooted from its

open network structure is possible in ambient conditions [16-19]. Further deformation of the amorphous silica following densification results in crack initiation and brittle fracture. On the other hand, at temperatures near glass transition temperature, the amorphous silica can obtain sufficient energy to break the interatomic bonds. Based on this, silica can accommodate large plastic deformation through thermally activated homogeneous shear flow, of which the interatomic bond switching is a main mechanism. If the densification is the main deformation mechanism, the uniaxial compression test will only leave a dent on the sphere along the loading direction. However, if the thermally activated shear flow is the main deformation mechanism, the sphere will expand in the transverse direction of the loading direction because the total volume should remain constant. SEM images of the compressed silica sphere up to 140nm clearly shows this tendency. Compressed silica sphere without E-beam exhibits a meridian crack induced brittle fracture with the dent on the upper part of the sphere [20]. Diameter of the sphere is almost same as that of the uncompressed sphere, in that, the densification of the silica is the main deformation mechanism during compression without the E-beam. Compressed silica sphere under the 5 kV 200 pA E-beam shows almost pancake-like shape with transversely expanded diameter, which supports that the homogeneous shear flow becomes a dominant deformation mechanism under the E-beam irradiation. That is, the homogeneous shear flow can be activated by the E-beam rather than the thermal energy. Moreover, judging by the difference in the

compressed shape of the amorphous silica sphere under the various E-beam, the degree of the shear flow depends on the acceleration voltage and the current of the E-beam.

Load-indentation depth curves of the amorphous silica spheres under the various beam conditions reveal that the pancake-like deformed spheres not only exhibit higher indentation depths up to the same maximum load but also larger permanent deformation, compared to the beam off cases (Fig. 3.3). This E-beam induced permanent deformation changes sensitively with the acceleration voltage and the current of the E-beam and is evident even for small indentation depth ( $\sim 0.07$  strain) (Fig. 3.4). As the shear flow becomes dominant under the E-beam irradiation rather than the densification, it can be deduced that the permanent deformation is highly dependent on the degree of the shear flow. Furthermore, as can be seen from the load-displacement curves, the softer the material, the more permanent deformation, i.e. shear flow occurs. That is, it is possible to estimate the degree of shear flow induced by the E-beam by comparing the degree of mechanical softening of the silica sphere under the various E-beam conditions.

We defined a dimensionless parameter that can quantify the degree of softening from the load-indentation depth curves. High degree of the mechanical softening appears as a high indentation depth on the load-indentation depth curve. However, owing to the geometrical difference in the initial and the compressed shape of each silica spheres, simply comparing the

indentation depth cannot reveal the degree of softening. We tried to avoid this problem by setting the dimensionless parameters based on the flow stress at 0.1 strain in the engineering stress-engineering strain curves. The dimensionless softness parameter is expressed as

$$K_{softness\ parameter} = \frac{\sigma_{0.1\ strain}}{E_{bulk} \cdot \varepsilon}, \quad (3.1)$$

where  $\sigma_{0.1\ strain}$  is the flow stress at 0.1 engineering strain,  $\varepsilon$  is 0.1 engineering strain, and  $E_{bulk}$  is the known elastic modulus of the amorphous silica (71 GPa). The softer the material, in other words, the greater the degree of the E-beam induced shear flow, the smaller the parameter.

Fig. 3.5 (a), (b) show the softness parameters of the silica sphere compressed under the various E-beam conditions. For the compression test under the E-beam with 1 kV acceleration voltage, the softness parameters are almost the same, regardless of the beam current, as those of the tests without the E-beam. In that, the 1 kV acceleration voltage E-beam cannot trigger the homogeneous shear flow during the compression test. On the other hand, when the acceleration voltage is 2kV or more, a clear mechanical softening of the amorphous silica sphere can be confirmed. When the beam current is constant, the mechanical softening increases with the acceleration voltage up to 5 kV, and the opposite tendency in the mechanical softening appears when the acceleration voltage is larger than 5 kV. Considering that the acceleration voltage of the E-beam corresponds to the energy of electrons, the mechanical



softening phenomenon does not seem to be proportional to the incident electrons' energy. For the correlation between the mechanical softening phenomenon and the beam current, as confirmed from the softening parameter, similar tendency is observed among the various acceleration voltages, except the 1 kV cases. As the beam current increases, the degree of the mechanical softening increases, and at 100 pA or higher, the softening degree becomes saturated. To confirm whether this saturation tendency at the high beam current is due to the sol-gel method based fabrication process which develops a large number of defects including silanol groups in the material, we performed the in-situ compression test on amorphous SiO<sub>2</sub> pillars with 280 nm diameter and 900 nm height fabricated from a hydrothermally grown substrate. The E-beam induced deformation behaviors also occur even for the amorphous SiO<sub>2</sub> pillar (Fig. 3.6 (a), (b)). In addition, there is a similar dependency on the beam current just like the silica spheres (Fig. 3.6 (c)). That is, the mechanical softening and the plastic deformation by the shear flow of the amorphous silica is obviously possible even under the low energy E-beam conditions at the SEM, and also this phenomenon does not depend on the geometry or the fabrication process. Next, in order to clarify the acceleration voltage and the beam current dependency of the E-beam induced mechanical softening phenomenon, we analyzed how the electrons in the beam and atoms in the silica sphere interact.

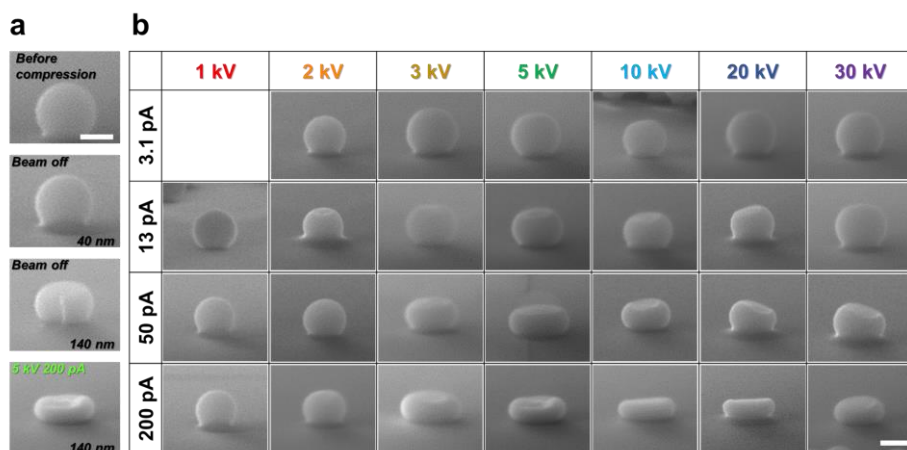


Figure 3.2 SEM images of the amorphous silica sphere before and after compression under various e-beam conditions. (a) Compressed amorphous silica spheres up to various indentation depths with/without the e-beam. (b) Compressed amorphous silica spheres up to 100 $\mu$ N under various e-beam conditions. Scale bars indicate 200 nm.

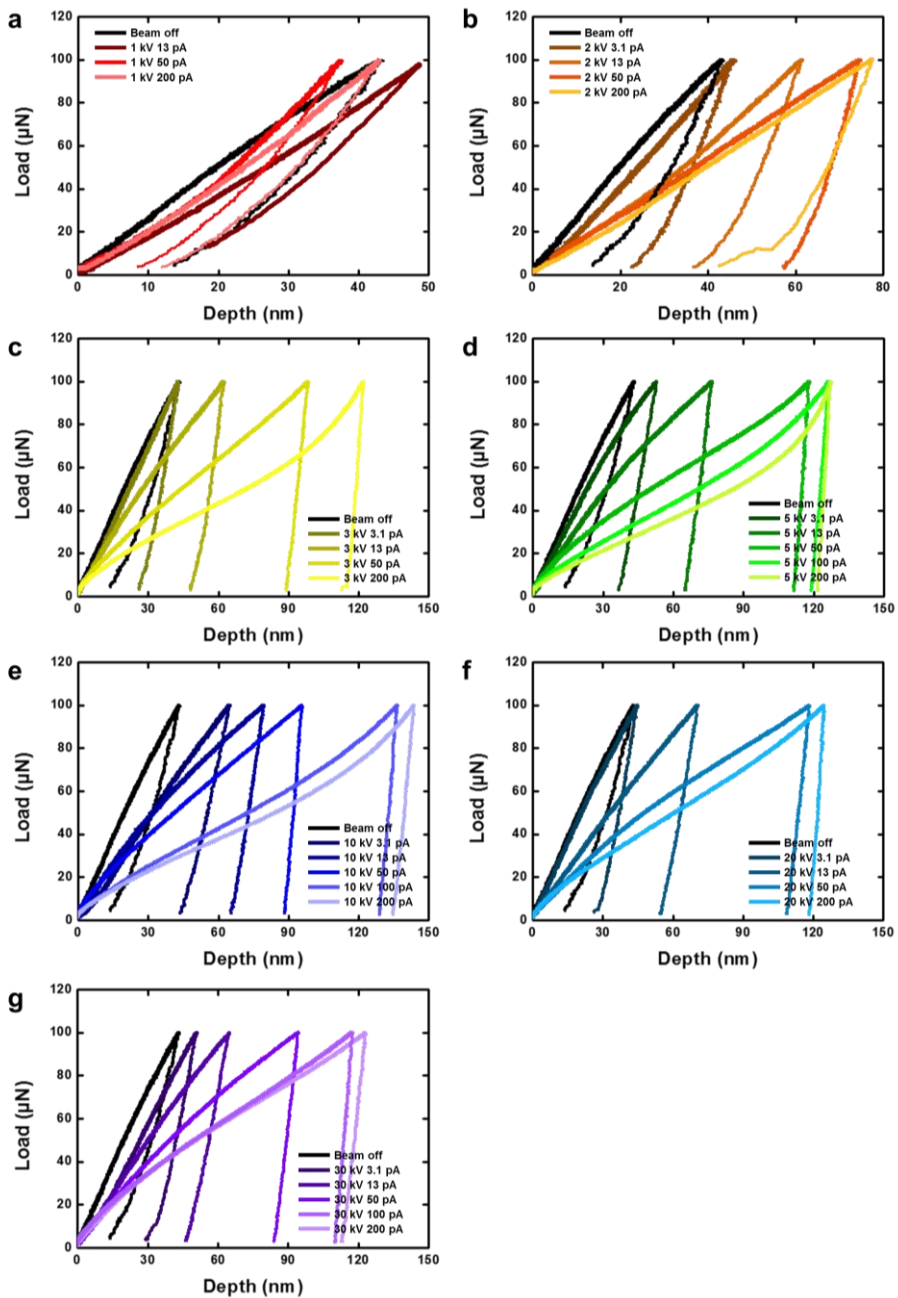


Figure 3.3 Load-indentation depth curves of the amorphous silica sphere compression test up to  $100\mu\text{N}$  under various e-beam conditions.

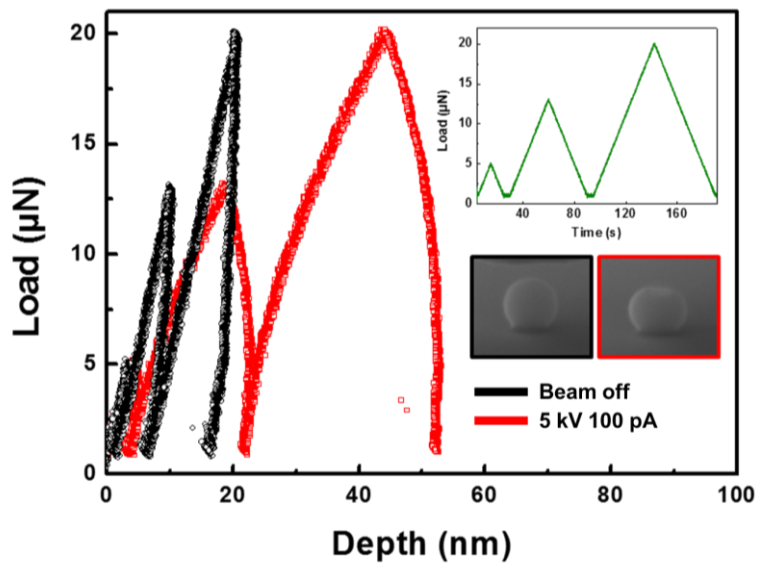


Figure 3.4 Load-indentation depth curves of the amorphous silica sphere compression test up to  $20\mu\text{N}$  with/without the E-beam. Black and red color indicates the results without and with the E-beam, respectively.

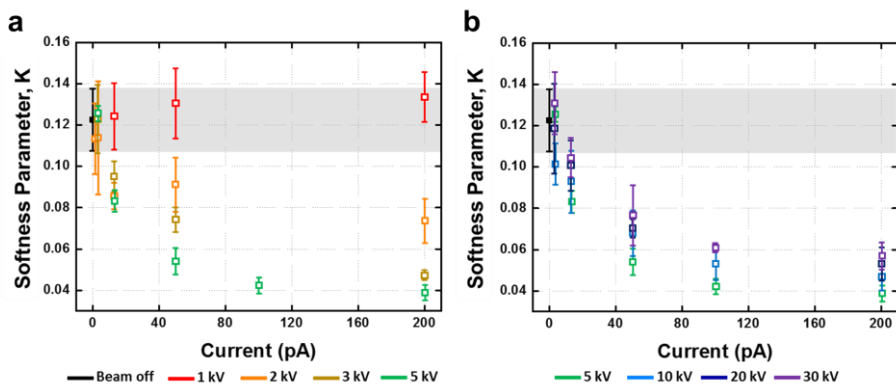


Figure 3.5 Softness parameters of the amorphous silica spheres calculated from the load-displacement curve of the compression tests under the various e-beam conditions.

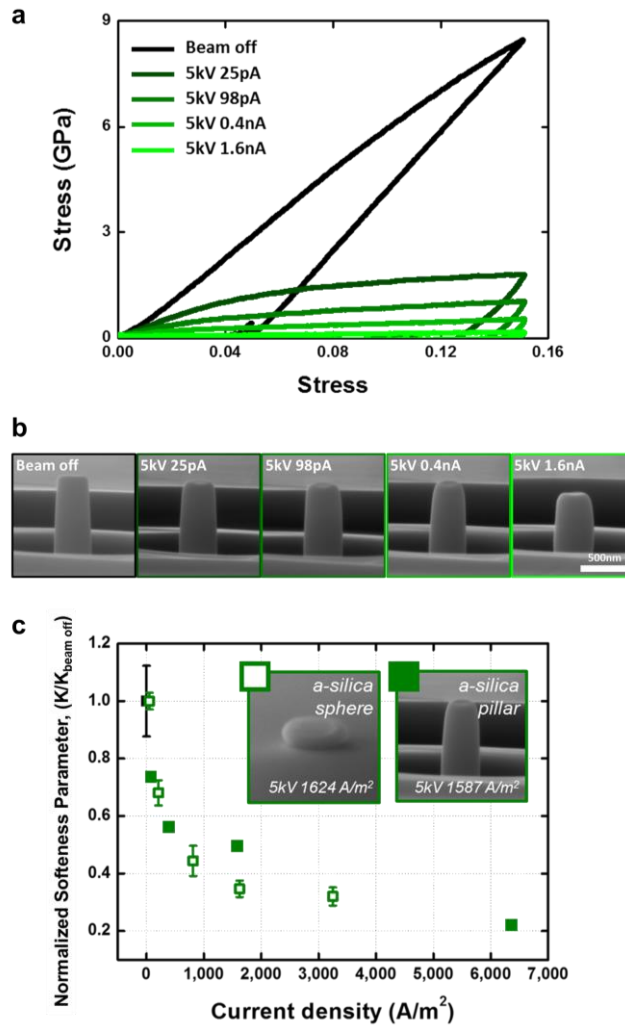


Figure 3.6 In-situ compression tests of the fused silica pillar under the e-beam with 5 kV acceleration voltage. (a) Engineering stress-Engineering strain curves of the compression tests. (b) SEM images of the compressed pillars. (c) Plotted normalized softness parameters of the compressed fused quartz pillars with those of the compressed amorphous silica sphere. Scale bars indicate 200 nm.

### 3.3.2 Interaction between the incident electrons and the amorphous silica sphere

The incident electrons in the material interact with matter through elastic and inelastic scattering. During the elastic scattering, the energy of the electron remains constant, but the electron deviates from its original trajectory. On the other hand, for the inelastic scattering, the electron maintains its trajectory, but loses its energy [21, 22]. Simulating the elastic and inelastic scattering of incident electrons within the amorphous silica provides an approximate grasp of the E-beam induced deformation behaviors.

We constructed an electron-material interaction model that reflects the geometry of the silica sphere and the actual E-beam irradiation conditions including the acceleration voltages and the beam currents in this research through a monte-carlo simulation method (CASINO (Ver. 3.3)). The density and work function of the amorphous silica were set at  $2.2 \text{ g/cm}^3$  and  $9.9 \text{ eV}$ , respectively. In the model, the focus of the E-beam with the beam diameter of  $3 \text{ nm}$ , which is consistent with the SEM in this research, is on top of the amorphous silica sphere. This model simulates how the silica sphere interacts with the incident electrons during the E-beam irradiation. Fig. 3.7 (a) shows the energy absorbed by the amorphous silica sphere from the incident electrons. According to the simulation results, the absorbed energy is proportional to the number of electrons, that is, the beam current. Moreover, the absorbed energy also shows maximum values at  $3 \text{ kV}$  acceleration voltage among the various acceleration voltages. However, unlike the softening parameter, the absorbed

energy does not saturate at high current, and the acceleration voltage which shows the most prominent softening (5 kV) does not match with the acceleration voltage at which the silica sphere absorbs the highest energy (3 kV).

The low correlation between the mechanical softening phenomenon and the absorbed energy leaves room for another possible factor, a volume interacting with the E-beam in the silica sphere. The interacting volume can be extracted from the energy-absorbed region of the silica sphere. Since the softening parameter, strictly speaking, is inversely proportional to the degree of mechanical softening, we focused on the volume which does not interact with the E-beam in the silica sphere. The non-interacting volume fraction is expressed as

$$f_{\text{Noninteracting volume fraction}} = 1 - \frac{V_{\text{interact}}}{V_{\text{sphere}}}, \quad (3.2)$$

where  $V_{\text{interact}}$  is the interacting volume extracted from the model, and  $V_{\text{sphere}}$  is the volume of the amorphous silica sphere. Fig. 3.7 (b) plots the non-interacting volume fraction of the silica sphere with various E-beam conditions that were used during the in-situ compression tests. Remarkably, the non-interacting volume fraction exhibits a very similar tendency to the softening parameter (Fig. 3.5 (a, b)). First, when the number of incident electrons is constant, the non-interacting volume fraction continues to decrease until 5 kV acceleration voltage, but after 10 kV, the opposite tendency emerges. Fig. 3.7 (c) shows the



trajectory of the incident electrons corresponding to 13 pA beam current as viewed from the cross section of the silica sphere. From 1 kV to 5 kV acceleration voltage, the incident electrons propagate with a large scattering angle inside the silica sphere. For the E-beam with 1 kV acceleration voltage, it penetrates only about 40 nm due to its low energy. However, for the E-beam with 5 kV acceleration voltage, electrons have sufficient energy to penetrate the entire silica sphere, so that the interacting volume is evenly distributed throughout the sphere, resulting in a low non-interacting volume fraction. When the acceleration voltage is more than 10 kV, the scattering angle becomes smaller, and the interacting volume is intensively developed along the E-beam's incidence direction. Eventually, the E-beam with high acceleration voltage generates a higher non-interacting volume fraction than the E-beam with 5 kV acceleration voltage despite the high-enough energy to penetrate the amorphous silica sphere. For this reason, the interacting volume is not simply proportional to the E-beam energy but is the largest at the acceleration voltage of 5 kV. In addition, since the geometry is limited to the 280 nm diameter sphere rather than a semi-infinite medium, the interacting volume cannot linearly increase in proportion to the beam current. Fig. 3.7 (d) shows the trajectory of the incident electrons corresponding to 100 pA beam current with 5 kV acceleration voltage, and clearly described the saturation of the interacting volume inside the silica sphere. The non-interacting volume fraction and the softening parameter show a very similar dependency on the acceleration voltage and the beam current.

That is, the E-beam induced deformation behaviors of the silica sphere can be explained in the point view of the interacting volume.

To verify the validity of the explanation based on the interacting volume, we performed additional compression tests. The interacting volume can be differed by the size of the E-beam irradiation area, or the pixel size. That is, a pixel size dependency of the E-beam induced deformation behaviors can support the validity of the interacting volume. Before looking into this, in order to determine the number of pixels to consider, one should investigate the scan rate (E-beam dwell time on each pixel) dependence of the E-beam induced deformation behavior. We performed the compression test on the silica pillars with various scan rate under the E-beam of 5 kV and 18 kV acceleration voltages. As shown in Figure 3.8, the E-beam induced deformation behavior under 5 kV and 18 kV show no scan rate dependency. As the time scale of the E-beam induced deformation behaviors is smaller than 100 nsec, the number of pixels we need to consider for the pixel size dependency of the E-beam induced deformation behavior is only one.

Figure 3.9 shows the pixel size dependency of the E-beam induced deformation behaviors of the silica pillars with various pixel sizes. Both 5 kV and 18 kV E-beams are least effective on the deformation behavior when the pixel size is smallest ( $0.02 * 0.02 \text{ nm}^2$ ). For the E-beam of 5 kV acceleration voltage, the same E-beam induced deformation behaviors are observed when

the pixel size is bigger than  $0.04 * 0.04 \text{ nm}^2$ . On the other hand, for the E-beam of 18 kV acceleration voltage, as the pixel size increases, the E-beam effect on the deformation behavior becomes prominent. As shown in Figure 3.7 (c), the E-beam of 5 kV acceleration voltage is expected to show the evenly distributed interacting volume inside the silica sphere. It can be expected that evenly distributed interacting volume will not change much even if the pixel size changes. However, for the acceleration voltages more than 10 kV, the interacting volume is intensively developed along the E-beam's incidence direction. The interacting volume is strongly dependent on the pixel size and increases as the pixel size increases. As a result, the pixel size dependency of the E-beam induced deformation behaviors under the 5 kV and 18 kV E-beam well supports the validity of the interacting volume.

Silica nanoshell structures are also useful for verifying the interacting volume of the electron beam with the amorphous silica. We fabricated 20 nm thickness silica nanoshell spheres and performed the in-situ compression test under the E-beam with 1 kV and 30 kV acceleration voltages (Fig. 3.10). When the silica nanoshell sphere is compressed without the E-beam, only the brittle fracture, same as the solid sphere, is observed. Moreover, the E-beam induced mechanical softening and permanent deformation of the silica nanoshell sphere emerges during the in-situ compression test under the E-beam with 30 kV acceleration voltage. The notable point is that the nanoshell sphere the same E-

beam induced deformation behaviors during the compression test under the irradiation of 1 kV E-beam which penetrates only about 40 nm into the silica solid sphere.

Strain rate sensitivity and activation volume provide information of the rate limiting process during plastic deformation, that is, a dominant deformation mechanism. We investigated strain rate sensitivity and activation volume by performing in-situ compression test on the fused silica pillars at four different strain rates (0.0006, 0.002, 0.006, 0.014 s<sup>-1</sup>). In Fig. 3.11, unlike the compression tests without the E-beam where there is almost no change in the engineering stress-engineering strain curves due to the strain rates, the curves of the compression tests with the E-beam irradiation changes remarkably. The strain rate sensitivity ( $m$ ) can be calculated as,

$$m = \frac{\partial \ln \sigma_f}{\partial \ln \dot{\epsilon}}, \quad (3.3)$$

where  $\sigma_f$  is the flow stress at 0.15 strain, and  $\dot{\epsilon}$  is the strain rate of the in-situ compression tests. Regardless of the strain rate, the flow stress at 0.15 strain is the highest for beam off compression test, and is the lowest when the compression test is conducted under the E-beam with 5 kV acceleration voltage (Fig. 3.12 (a)). The beam off compression tests exhibit the strain rate sensitivity of about 0.007 which is consistent with previous researches on the bulk amorphous silica at ambient conditions [23-25]. The strain rate sensitivity increases under the E-beam irradiation. Especially under the 5 kV E-beam

irradiation, the strain rate sensitivity reaches 0.273, which is 37 times larger than the beam off case. For amorphous materials, the strain rate sensitivity is a measure of the homogeneous deformation. As this value approaches zero, the material accommodates the plastic deformation through shear localization processes. On the other hand, as the strain rate sensitivity increases, the homogeneous deformation becomes dominant during the plastic deformation [26, 27]. Through strain rate sensitivity, it can be deduced that the amorphous silica sphere accommodates the plastic deformation through the homogeneous shear flow under the E-beam irradiation.

The plastic deformation mechanism can also be estimated through the activation volume. In case of the crystalline materials, the activation volume decreases as the deformation mechanism changes from dislocation slip to grain boundary sliding or diffusional creep [28, 29]. In the amorphous material, the activation volume refers to a volume of atomic cluster which migrates during plastic deformation [30]. One can expect that as the homogeneous deformation becomes dominant, the activation volume decreases. The activation volume is expressed as,

$$V^* = \sqrt{3}kT \left( \frac{\partial \ln \dot{\epsilon}}{\partial \sigma_f} \right), \quad (3.4)$$

where  $k$  is Boltzmann's constant,  $T$  is the temperature. As shown in Fig. 3.12 (b), the beam off compression tests show the activation volume of about 117.73  $\text{\AA}^3$ , which is consistent with a previous research [30]. The activation volume is

about  $7.48 \text{ \AA}^3$  under the 5 kV E-beam irradiation where the homogeneous shear flow is most dominant. It can be expected that the incident electrons affect the interatomic bond switching mechanism and makes it easier to occur. As a result, the size of the mobile atomic cluster during the plastic deformation gets smaller than the intrinsic value ( $117.73 \text{ \AA}^3$ ). The relatively large activation volume of the compression tests under the 2 kV and 18 kV E-beam ( $13.01 \text{ \AA}^3$  for 2 kV and  $8.31 \text{ \AA}^3$  for 18 kV) is consistent with the noninteracting volume fracture calculation obtained from the monte-carlo simulation. The incident electrons into the material affects the interatomic bond switching mechanism, and that the homogeneous shear flow deformation occurs even under the E-beam irradiation. These results also verify that the E-beam induced deformation behaviors are strongly related to the interaction volume between the incident electron and the silica sphere, which varies depending on the acceleration voltage and the beam current of the E-beam.

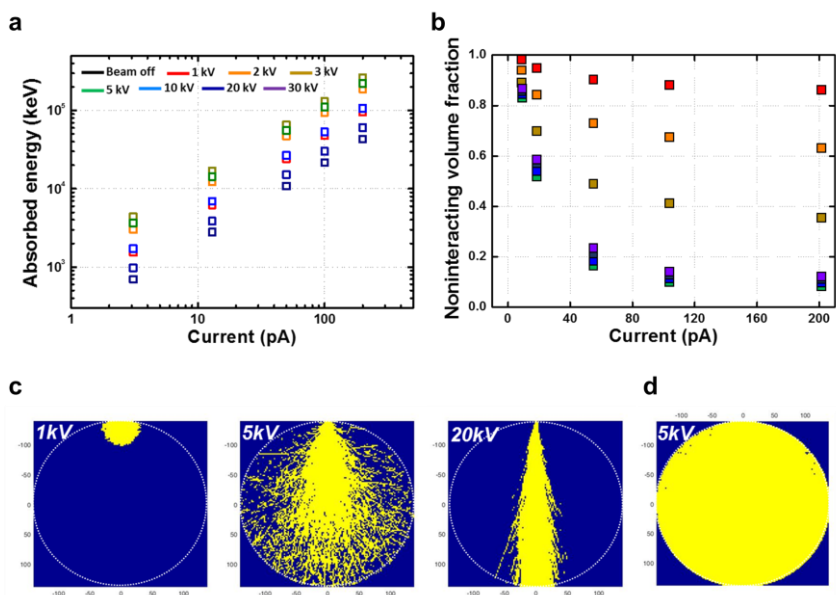


Figure 3.7 Interaction between the incident electrons and the amorphous silica sphere. (a) Absorbed energies by the amorphous silica sphere from the e-beam. (b) Non-interacting volume fractions inside the amorphous silica sphere under the various e-beam conditions. (c) Interacting volume induced by 13 pA E-beam as viewed from the cross-section of the amorphous silica sphere. (d) Interacting volume induced by 5 kV 100 pA E-beam as viewed from the cross-section of the amorphous silica sphere. Interacting and non-interacting area are indicated as yellow and blue color, respectively.

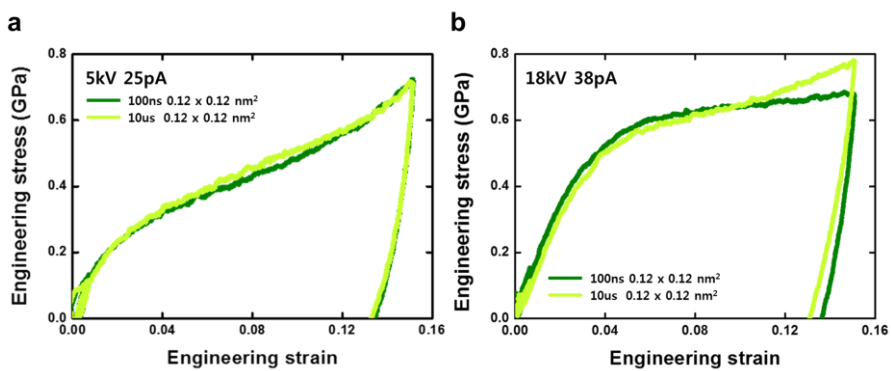


Figure 3.8 Scan rate dependency of the E-beam induced deformation behavior of the silica pillars. Engineering stress-engineering stress curves of the compression tests under the E-beam of 5 kV (a) and 18 kV (b) acceleration voltages.



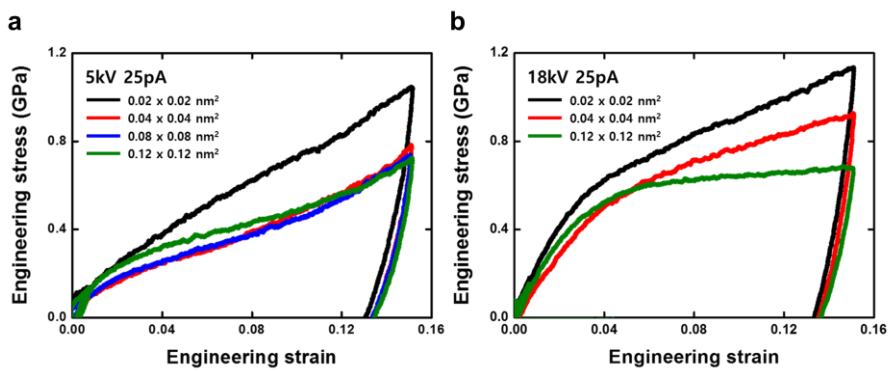


Figure 3.9 Pixel size dependency of the E-beam induced deformation behavior of the silica pillars. Engineering stress-engineering stress curves of the compression tests under the E-beam of 5 kV (a) and 18 kV (b) acceleration voltages.

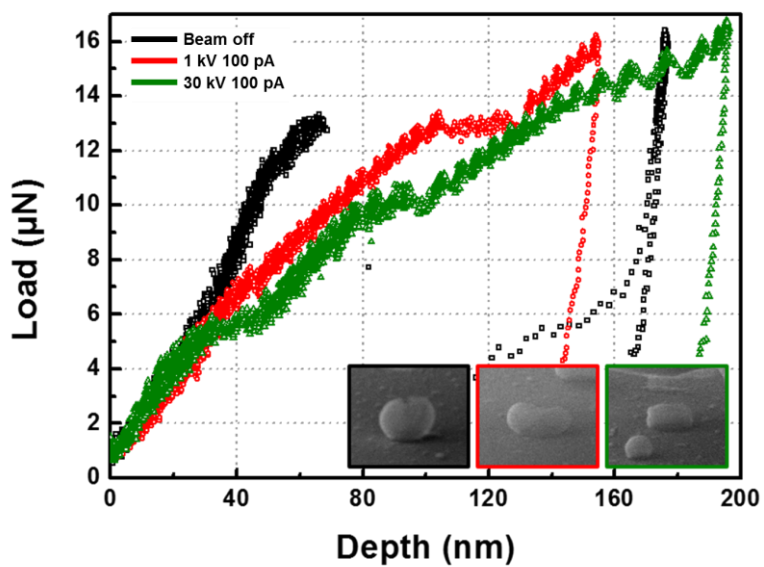


Figure 3.10 Load-displacement of the in-situ compression test of the amorphous silica nanoshell sphere with/without the E-beam. Insets indicate the SEM images of the compressed nanoshell spheres.

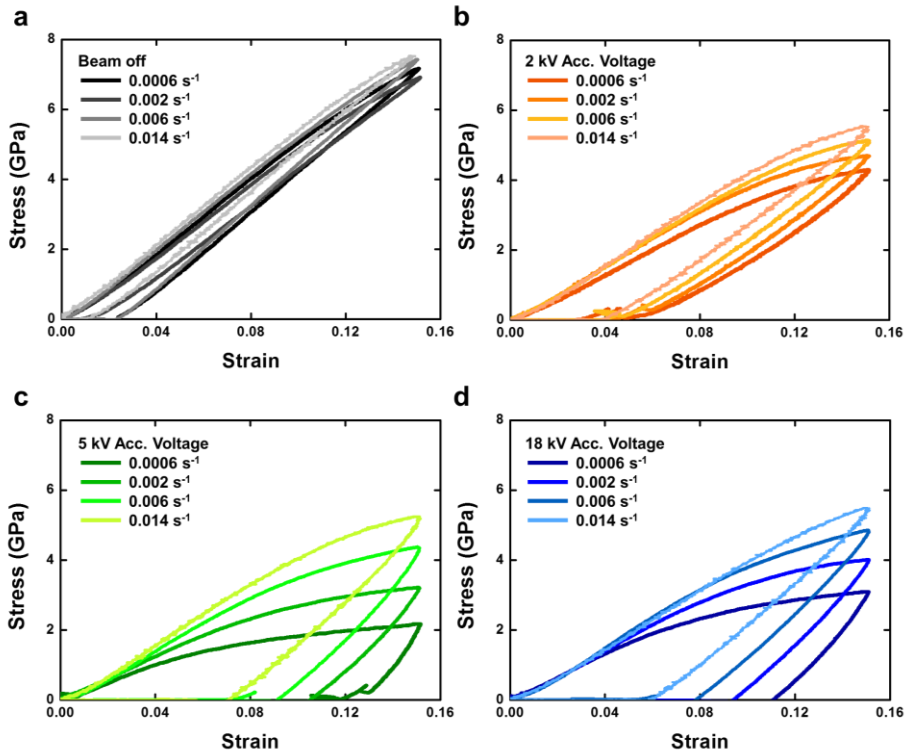


Figure 3.11 Engineering stress-engineering strain curves of the in-situ compression test of fused quartz pillars at 0.0006, 0.002, 0.006, 0.014 s<sup>-1</sup> strain rate under (a) beam off , (b) 2 kV E-beam, (c) 5 kV E-beam, and (d) 18 kV E-beam conditions

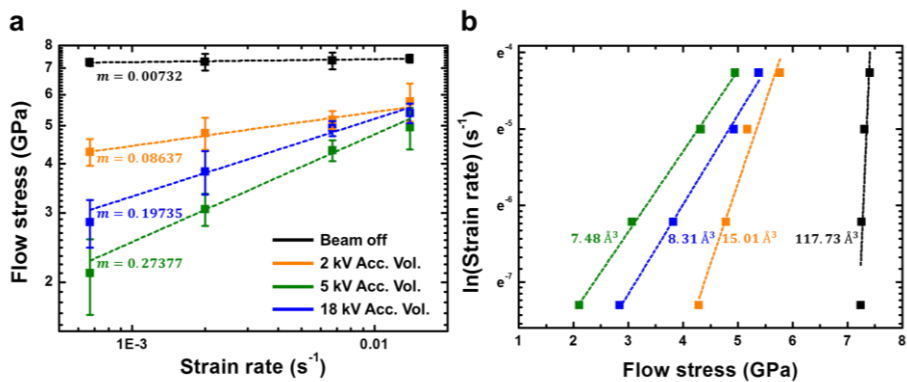


Figure 3.12 Compression test with various strain rates under 2 kV, 5 kV, 18 kV acceleration voltage e-beams. (a) Strain rate sensitivity and (b) activation volume plot of the fused quartz pillars. Black, orange, green, blue colors indicate compression test under no e-beam, 2 kV, 5 kV, and 18 kV acceleration voltage e-beam respectively.

### 3.3.3 E-beam effect on deformation behavior of other amorphous ceramics

To induce the homogenous shear flow of the amorphous ceramic materials, sufficient energy to break and switch the interatomic bonds is essential. This is why the homogeneous shear flow is only thermally activated at high temperatures above 1000 °C. The energy of the E-beam in SEM is more than three orders of magnitude higher than the Si-O bond (3 to 4 eV), and this energy is high enough to affect the Si-O bonds in the amorphous silica. This is consistent with the relationship between the mechanical softening phenomenon and the interaction volume as analyzed above. The incident electrons into the silica sphere directly affect the Si-O bond nature and the interatomic bond switching mechanism [5-7, 22]. As a result, a deformation behavior mimicking the thermally activated homogeneous shear flow emerges under the E-beam irradiation.

As the E-beam activates the mechanical softening and the plastic deformation by mimicking the thermally activated homogeneous shear flow, other amorphous ceramic materials may also be expected to exhibit the similar phenomenon under the E-beam irradiation. Amorphous  $\text{Al}_2\text{O}_3$  and amorphous  $\text{TiO}_2$  pillars fabricated by a deposition and the focused ion-beam (FIB) milling processes also show the similar mechanical softening and the shear flow deformation behavior with the amorphous silica during the compression test under the E-beam (Fig. 3.13). The degree of mechanical softening of the amorphous  $\text{Al}_2\text{O}_3$  and  $\text{TiO}_2$  may not be the same with the amorphous silica,

since the shear flow varies depending on the bonding nature, fragility, and coordination number of the material. However most importantly, we confirmed that the mechanical softening and the shear flow can possibly be triggered by the E-beam not only the amorphous silica, but also various amorphous ceramics, including the  $\text{Al}_2\text{O}_3$  and  $\text{TiO}_2$ .

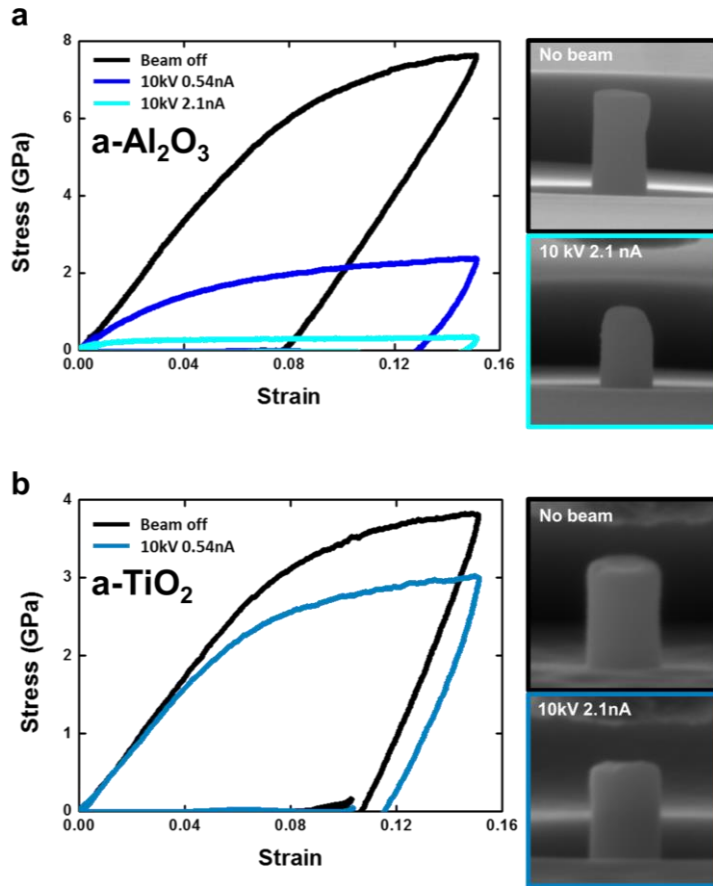


Figure 3.13 Engineering stress-engineering strain curves of the in-situ compression test of amorphous ceramics: (a) amorphous  $\text{Al}_2\text{O}_3$ , (b) amorphous  $\text{TiO}_2$ . Insets indicate the compressed amorphous ceramic pillars.

### **3.4 Electron-beam effect on deformation behavior of crystalline ceramics**

How does the E-beam affect the deformation behavior of crystalline ceramics? Crystalline ceramics have their own slip system, but due to their high activation energy, the plastic deformation rarely occurs in the ambient conditions. Because there is no shear flow mechanism for crystalline ceramics, dislocation nucleation and migration are essential to induce the plastic deformation. Although the E-beam can affect the interatomic bonds in the material and even break the bonds, it is almost impossible to generate 1-dimensional line defects such as dislocation. Therefore, it is expected that the similar E-beam induced deformation behavior with the amorphous ceramics will be difficult to occur in the crystalline ceramics.



### 3.4.1 E-beam effect on deformation behavior of crystalline ceramics

To investigate the E-beam irradiation effect on the crystalline ceramics, we performed the in-situ compression test on the crystalline SiO<sub>2</sub> (alpha quartz, (0001)), Al<sub>2</sub>O<sub>3</sub> (alpha alumina, (0001)), TiO<sub>2</sub> (Rutile, (001)), and ZnO (001) pillars. Crystalline Al<sub>2</sub>O<sub>3</sub>, TiO<sub>2</sub>, and ZnO pillars show the same engineering stress-engineering strain curves with or without the E-beam, respectively (Fig. 3.14). Only the SiO<sub>2</sub> surprisingly exhibits the E-beam induced deformation behavior during the in-situ compression test (Fig. 3.15). Moreover, the deformation behavior of the SiO<sub>2</sub> also shows the beam current dependency just like the amorphous ceramics does; as the current increases, the SiO<sub>2</sub> softens and the permanent deformation also increases. Unlike the amorphous ceramics, however, the engineering stress-engineering strain curve of the E-beam affected SiO<sub>2</sub> pillar increases linearly followed by the maximum stress, and then falls into the plateau. As shown in the SEM image of the compressed pillar without the E-beam, only the upper part of the pillar is slightly distorted. However, in the presence of the E-beam, the region expanding in the transverse direction gradually increases as the beam current increases (Fig. 3.16).

We investigated the microstructural information of the transversely expanded region of the compressed SiO<sub>2</sub> pillar through the TEM dark field image analysis (Fig. 3.17). Cross section dark field image of the pillar before compression test shows a white-colored core with a 50 nm-thickness black-colored shell. As shown in the SAED pattern of each area, the bright white-

colored core and the black-colored shell correspond to the single crystalline and the amorphous SiO<sub>2</sub>, respectively. Compared to the pillar before compression, the amorphous area of the compressed pillars keep increases as the beam current increases. Considering this with the SEM images reveals that the transversely expanded parts of the compressed pillars correspond to the region where the phase transformation from the crystalline to amorphous phase occurred. Moreover, from the SEM snapshot images of the in-situ compression test up to 0.15 engineering strain under the 5 kV 0.4 nA e-beam irradiation, the pillar, keeping its original shape, deforms along the loading direction up to 0.08 strain. After 0.08 strain, the pillar expands in the transverse direction and the entire geometry is severely distorted (Fig. 3.18). By performing additional in-situ compression tests up to 0.04, 0.08, and 0.12 engineering strains under the E-beam of 0.4 nA beam current with 5 kV acceleration voltage, we rigorously investigated and linked the engineering stress-engineering strain curve and the microstructure of the single crystalline SiO<sub>2</sub> pillar. A perfect match between the engineering stress-engineering strain curves of the compression tests up to each maximum strain supports that the microstructure change at different engineering strain should be in the same tendency (Fig. 3.19). As shown in Fig. 3.20, every compressed pillars up to each maximum strains contains both crystalline and amorphous phases. More noteworthy is that the amorphized area of the compressed pillar is relatively small for the compression test of 0.04 maximum strain, but the amorphized area markedly increases when the

maximum strain is greater than 0.08. As the maximum stress of the engineering stress-engineering strain curve of the compressed pillar under the 0.4 nA 5 kV E-beam appears at the 0.08 engineering strain, the peak stress is possibly related to the threshold stress of the amorphization of the crystalline SiO<sub>2</sub>. In addition, as the severely deformed amorphized region of the compressed pillar up to 0.15 engineering strain suggests, the higher the strain, the more deformation occurs in the amorphized region of the compressed SiO<sub>2</sub> pillar. The amorphization and the mechanical softening of the amorphized region during the in-situ compression test are expressed as the peak stress and the plateau in the engineering stress-engineering strain curve, respectively.

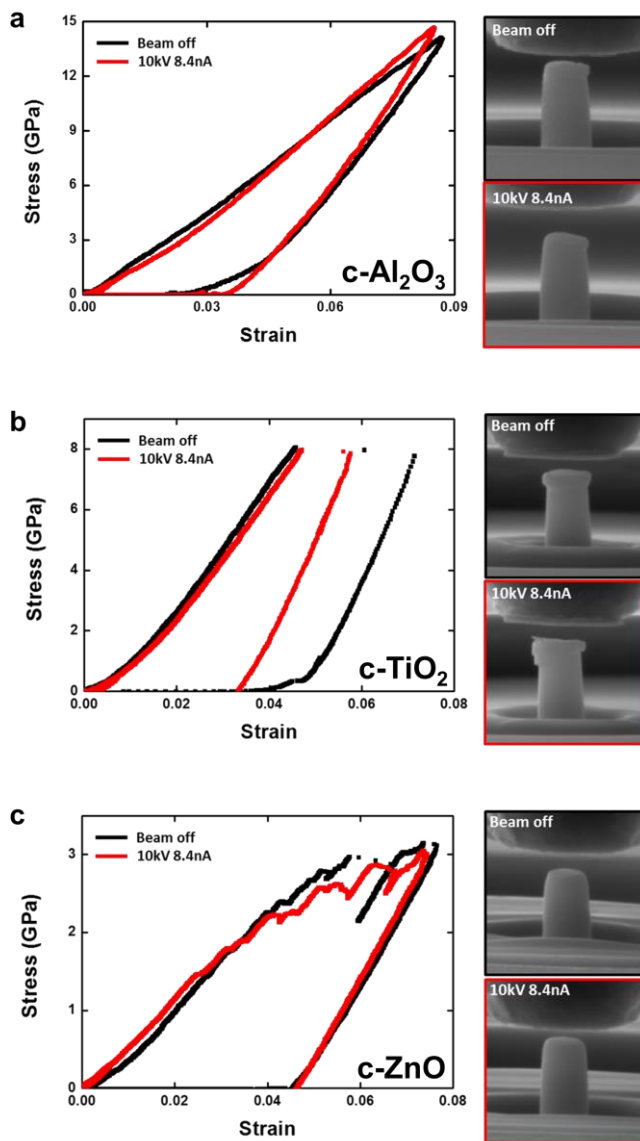


Figure 3.14 Engineering stress-engineering strain curves of the in-situ compression test of crystalline ceramics: (a) crystalline Al<sub>2</sub>O<sub>3</sub>, (b) crystalline TiO<sub>2</sub>, (c) crystalline ZnO Insets indicate the compressed amorphous ceramic pillars.

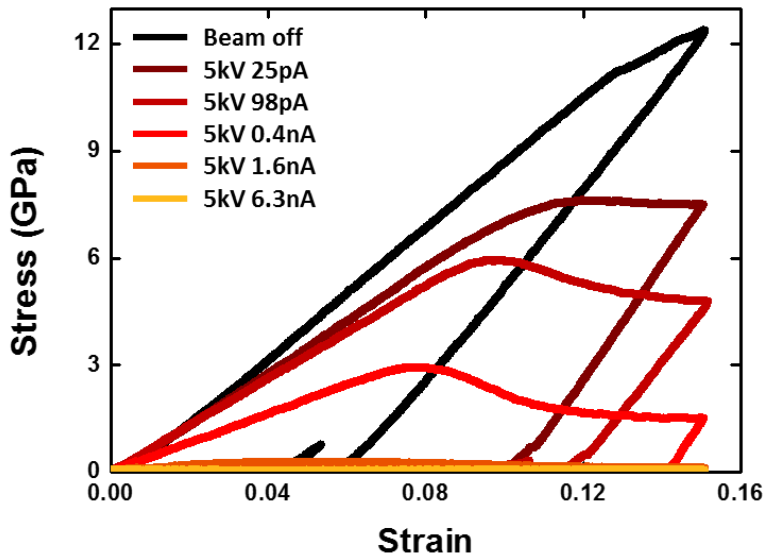


Figure 3.15 Engineering stress-engineering strain curves of the in-situ compression tests of the c-SiO<sub>2</sub> pillars under the 5 kV e-beam.

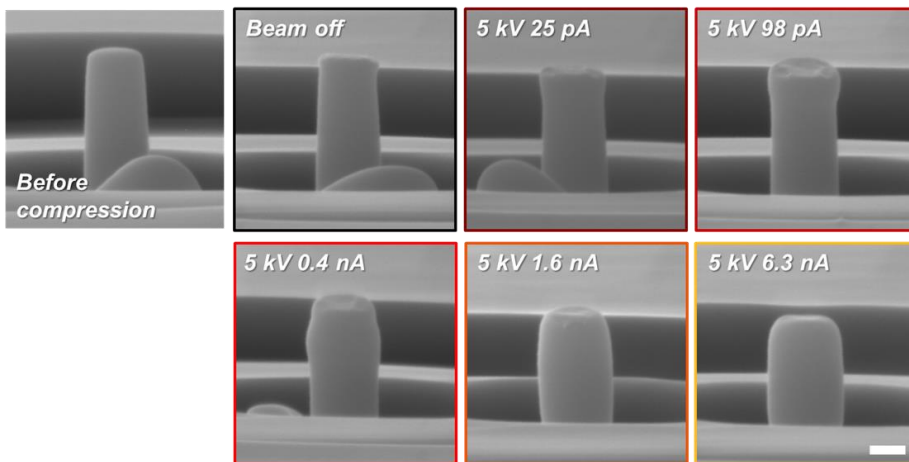


Figure 3.16 SEM images of the compressed c-SiO<sub>2</sub> pillars under the 5 kV e-beam. Scale bar indicates 200 nm.

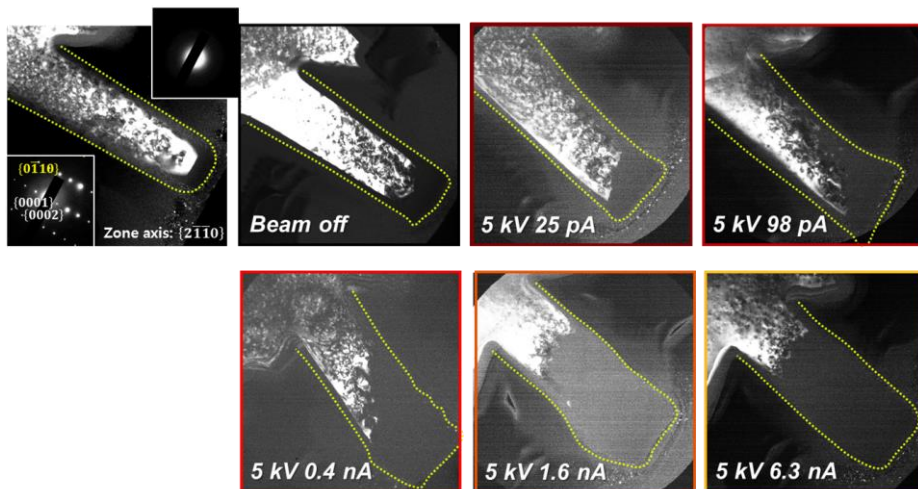


Figure 3.17 TEM dark field images of the compressed c-SiO<sub>2</sub> pillars under the 5 kV e-beam. Bright white and dark area indicate the crystalline and the amorphous phase, respectively.

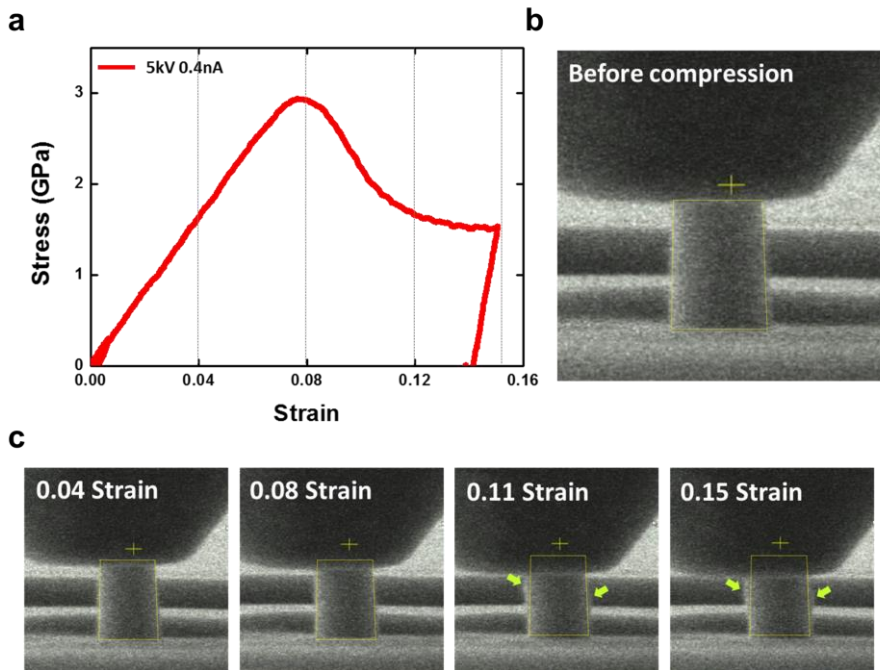


Figure 3.18 In-situ compression test of the crystalline SiO<sub>2</sub> pillar under 5 kV 0.4 nA e-beam. (a) Corresponding engineering stress-engineering strain curve. (b) Snap shot of the crystalline SiO<sub>2</sub> pillar before compression test. (c) Snap shot at each strain during the in-situ compression test.



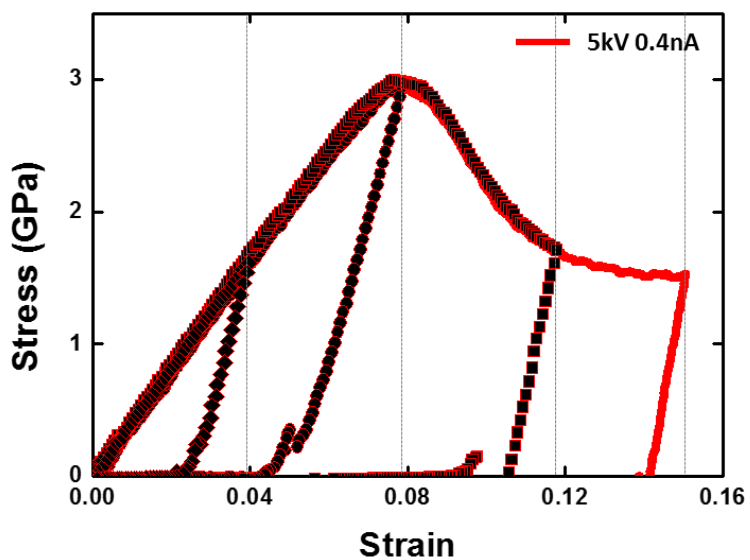


Figure 3.19 Engineering stress-engineering strain curves of the in-situ compression tests of the crystalline SiO<sub>2</sub> pillar under 5 kV 0.4 nA e-beam up to various maximum strains.

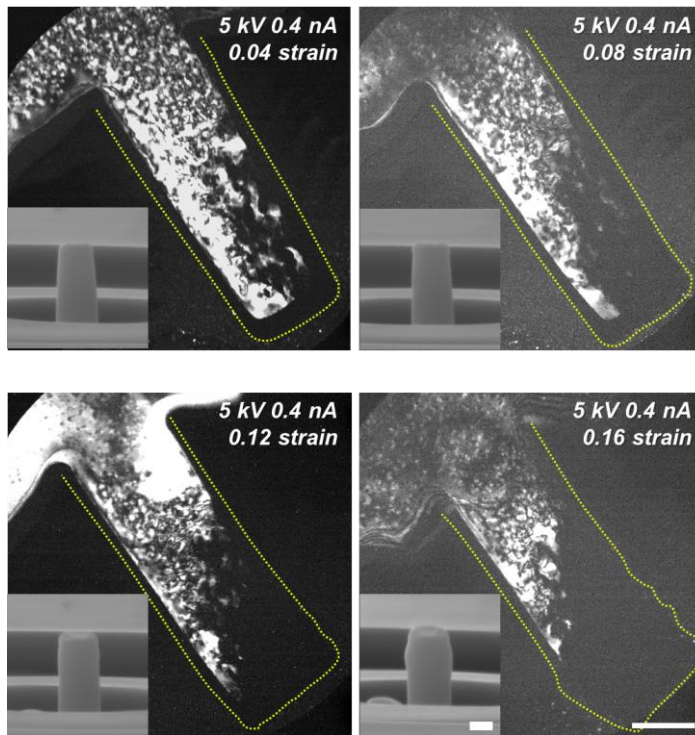


Figure 3.20 TEM dark field images of the compressed c-SiO<sub>2</sub> pillars under the 5 kV e-beam up to various maximum strains. Bright white and dark area indicate the crystalline and the amorphous phase, respectively. Scale bars indicate 200 nm.

### 3.4.2 Correlation between the e-beam affected deformation behavior and the atomic structures of the crystalline ceramics

Crystalline  $\text{SiO}_2$ , especially the alpha quartz, is an unconventional ceramic that undergoes the amorphization, which is the phase transformation from the crystalline to amorphous phase, when high pressure is applied [31-36]. This is due to its unique atomic structure. Generally, the crystalline ceramic materials possesses polyhedrons as a basic building blocks, and these composes entire atomic structures. In the case of the  $\text{Al}_2\text{O}_3$  and  $\text{TiO}_2$  which show no amorphization under the pressure,  $\text{AlO}_6$  and  $\text{TiO}_6$  octahedrons are the basic building blocks, respectively, and these octahedron are densely packed by sharing each surfaces. On the other hand, in the case of the crystalline  $\text{SiO}_2$ ,  $\text{SiO}_4$  tetrahedrons are loosely packed with sharing vertex, and also they link each other making up a double helix structure [37, 38]. This loosely packed double helix structure of the crystalline  $\text{SiO}_2$  allows to be twisted and compressed to accommodate the deformation when pressure is applied to it. When the applied pressure exceeds about 15 GPa, mutual penetration of  $\text{SiO}_4$  tetrahedrons occurs, and simultaneously Si atom makes another bond with O atom of the penetrating tetrahedron [31, 32, 34, 35]. That is, breaking periodicity by formation of new interatomic bond between Si and O atoms triggers the amorphization of the crystalline  $\text{SiO}_2$  under the pressure. In our case, the amorphization did occur at the upper part of the crystalline  $\text{SiO}_2$  pillar, even though there was no E-beam during the compression test. Using the ABAQUS

Standard (Ver. 6.10) general finite element analysis software, we established a 2D axisymmetric applied 4-node bilinear axisymmetric quadrilateral elements (CAX4) with adaptive meshes. We assumed that the crystalline SiO<sub>2</sub> exhibits a linear elastic deformation behavior. Through the finite element simulation, we confirmed that the high pressure of about 13.5 GPa, which is very close to the known-threshold pressure (15 GPa), in the upper part of the pillar is developed during the compression test (Fig. 3.21) [31, 32, 34, 35]. Under the E-beam irradiation, the threshold pressures of the amorphization, which corresponds to the highest stresses in the engineering stress-engineering strain curves, decrease very sensitively (Fig. 3.22). The pressure induced amorphization of the crystalline SiO<sub>2</sub> by inter-penetration of the SiO<sub>4</sub> tetrahedron must involve a large change in the O-Si-O bond angle [31-35]. In other words, the amorphization threshold pressure is directly related to the Si-O bond strength. Due to the inelastic scattering of the incident electrons, the nature of the interatomic bonds changes by an electronic excitation, and this could result in a bond weakening [5-7, 22]. It can be deduced that as the beam current increases, the number of the inelastic scattering increases, so the threshold pressure should also decrease. Summing up, the crystalline SiO<sub>2</sub> exhibits the E-beam affected deformation behavior in the form of decrease in the amorphization threshold pressure and the additional mechanical softening of the amorphized region.

Let us expand the concept of the E-beam effect on the deformation behavior induced by the change in the interatomic bond nature to the typical

ceramic materials. The trajectory of the incident electrons changes depending on the scattering events with the material. Should consider is that the interatomic bonds affected by the inelastic scattering arise randomly in the material. The amorphous and crystalline ceramics possess the thermally activated homogeneous shear flow and the dislocation slip as the plastic deformation mechanisms, respectively. Distinctively, the crystalline  $\text{SiO}_2$  additionally possesses the pressure induced amorphization as additional deformation mechanism due to its atomic structure. First, for densely packed crystalline ceramics such as  $\text{Al}_2\text{O}_3$ ,  $\text{TiO}_2$ , and  $\text{ZnO}$  etc. it is difficult to be amorphized under the pressure. Only way to make these crystalline ceramics deform plastically is nucleating the dislocations, but the randomness of the E-beam effect on the interatomic bond makes it impossible to generate such defect lines. Second, for the amorphous ceramics, as the interatomic bond switching is the key mechanism of the thermally activated homogeneous shear flow, a possibility of the E-beam effect on the deformation behavior is quite high. Third, for the crystalline  $\text{SiO}_2$  that can be amorphized under pressure, bending stress for the O-Si-O bonds depends on the Si-O bonding strength, so that the E-beam induced deformation behavior possibly occurs. The E-beam effect on the deformation behaviors of the ceramics is rooted from the atomic structure. This effect triggered by the scattering events between the incident electrons and the material results in the mechanical softening and the permanent deformation during the E-beam irradiation.

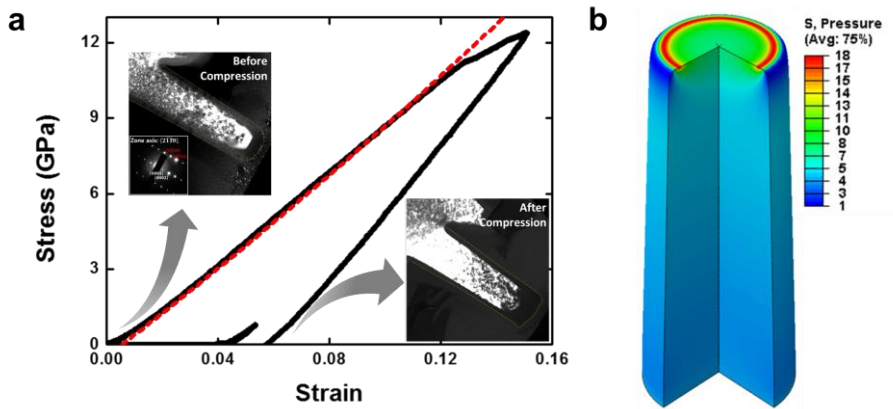


Figure 3.21 Amorphization threshold stress analysis. (a) Engineering stress-strain curve of the crystalline  $\text{SiO}_2$  pillar compressed without the e-beam. Red dotted line indicate the stress-strain curve of the crystalline  $\text{SiO}_2$  pillar assumed to be linearly elastic. Insets indicate corresponding TEM dark field images at each strains. (b) Pressure distribution when the experimental stress-strain curve deviates from the linearly elastic-assumed curve.

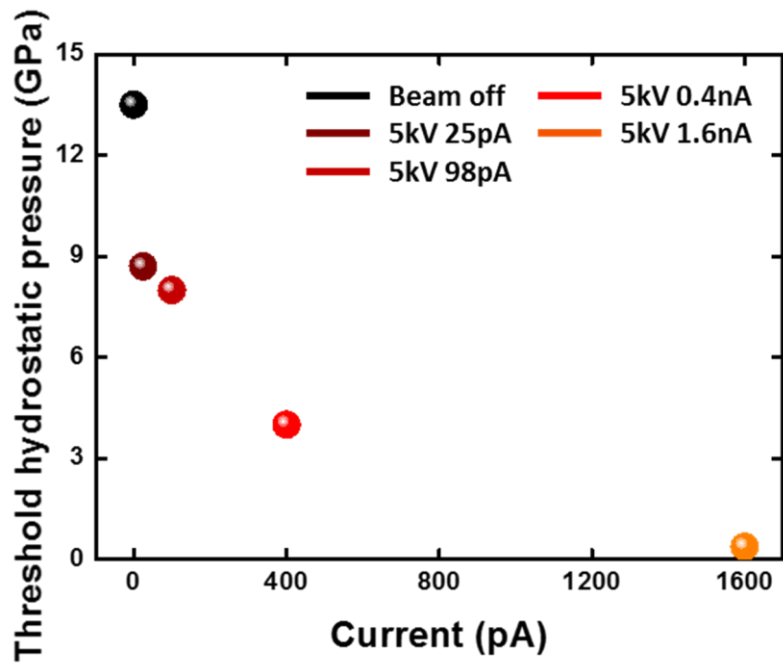


Figure 3.22 Plot of amorphization threshold hydrostatic pressure of the crystalline SiO<sub>2</sub> with beam current of the e-beam.

### **3.5 Nano-glasswork of the nano-ceramic material utilizing the E-beam irradiation**

If the E-beam induced deformation occurs, plastic deformation is possible even up to very high strain without any crack formation. This can provide an opportunity to open up new frontiers in the fabrication process of ceramic structural materials. Especially, since the amorphous ceramic cannot deform plastically in the ambient conditions, high temperature around the glass transition temperature is essential for the bulk scale fabrication processes. The situation is also the same in the nanoscale. However, since it is not easy to maintain such high temperature conditions in the nanoscale, the fabrication process has relied solely on simple deposition or synthesis processes. The geometry of the nanoceramics fabricated through these processes is limited to thin films, nanowires, and spheres. If we can mimic the thermally activated homogeneous shear flow in the nanoscale, it is possible to increase the degree of freedom in the geometry and fabrication process of the nanoceramics.

We propose a nano-glasswork utilizing the E-beam. The nano-glasswork means a mechanical forming of the amorphous ceramics in the nanoscale as if a bulk scale glasswork which is deforming the glass material freely at the high temperatures. Fig. 3.23 (a) shows three nano-glasswork we tried on the amorphous silica nanoshell sphere under the E-beam irradiation. First is compressing the nanoshell sphere uniaxially using the indenter (Fig. 3.10).



Under the E-beam, the silica nanoshell sphere deformed into the pancake-like shape along the indenter geometry without any crack formation. Second, we used three manipulators (Kleindeck, MM3A) installed in a FIB system (FEI, Quanta 3D) which can apply forces in various directions simultaneously, and mechanically deformed the silica nanoshell sphere. During applying forces, the silica shell spheres did not fracture in brittle manner and show excellent formability, even reminding of a ricecake-pounding (Fig. 3.23 (b)). Third, we made a small trench on the substrate using FIB milling and tried to plastically deform the silica nanoshell sphere by pushing it into the trench. Likewise, the silica shell sphere can be perfectly deformed and molded into the trench shape without any crack (Fig. 3.23 (c)). Simply irradiating the amorphous ceramics with the E-beam as the same effect as maintaining the high temperature. The nano-glasswork combining the mechanically applied force and the E-beam irradiation is fully feasible and has enormous potential.

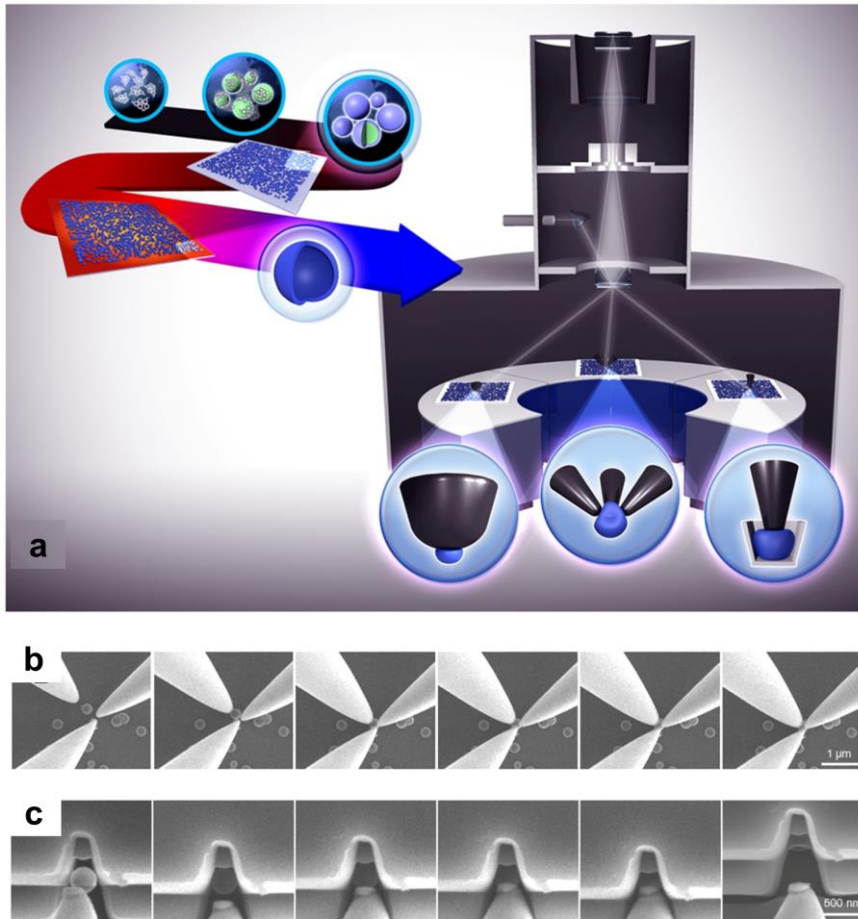


Figure 3.23 Nano-glasswork of the amorphous silica nanoshell sphere utilizing the E-beam irradiation. (a) Schematic diagram of the nano-glasswork with three different deformation methods. (b) Snap shots during the nano-glasswork by applying multi-axial loads to the nanoshell sphere with nano-manipulators. Scale bar indicate 1  $\mu\text{m}$ . (c) Snap shots during the nano-glasswork by molding the nanoshell sphere into the trench. Scale bar indicate 500 nm.

### 3.6 Conclusion

In this study, we investigated the E-beam induced mechanical softening and plastic deformation of the amorphous and crystalline ceramic materials ( $\text{SiO}_2$ ,  $\text{Al}_2\text{O}_3$ ,  $\text{TiO}_2$ ,  $\text{ZnO}$ ). We confirmed that the low energy electron-beam obviously trigger the mechanical softening and permanent deformation of the amorphous silica. This unusual deformation behavior also appears in the other amorphous ceramics including  $\text{Al}_2\text{O}_3$  and  $\text{TiO}_2$ . With computational analysis, it is confirmed that this electron-beam effect strongly depends on the interacting volume between the incident electrons and the material. For the crystalline ceramics, only the  $\text{SiO}_2$  shows the electron-beam induced deformation behavior, because of its unique atomic structure. Under the E-beam irradiation, the amorphization threshold pressure of the crystalline  $\text{SiO}_2$  reduces, and the amorphized  $\text{SiO}_2$  deforms further. On the other hand, there was no E-beam effect on the deformation behavior of other crystalline ceramics owing to their closely packed atomic structures. Finally, we proposed a new mechanical fabrication process for ceramic structural nanomaterials, namely, nano-glasswork which is deforming nanoceramics under electron-beam into certain shapes. Three different types of nano-glasswork were conducted on the amorphous silica nanoshell sphere. The nanoshell sphere perfectly deformed into desired shapes without any crack formation. This chapter presents a fundamental understanding on the E-beam induced deformation behavior of the

nanoceramics and a new mechanical process based on it. It is expected that this research will be a stepping stone for advanced manufacturing process for nanoceramics.

### 3.7 References

- [1] D. Jang, L.R. Meza, F. Greer, J.R. Greer, *Nat Mater*, 12 (2013) 893-898.
- [2] L.R. Meza, S. Das, J.R. Greer, *SCIENCE*, 345 (2014) 1322-1326.
- [3] L.R. Meza, A.J. Zelhofer, N. Clarke, A.J. Mateos, D.M. Kochmann, J.R. Greer, *Proc Natl Acad Sci U S A*, 112 (2015) 11502-11507.
- [4] S.G. Kang, D. Moon, J. Jang, J.Y. Kim, J.Y. Suh, E. Yoon, H.N. Han, I.S. Choi, *Nano Lett*, 18 (2018) 1323-1330.
- [5] K. Zheng, C. Wang, Y.Q. Cheng, Y. Yue, X. Han, Z. Zhang, Z. Shan, S.X. Mao, M. Ye, Y. Yin, E. Ma, *Nat Commun*, 1 (2010) 24.
- [6] M. Mačković, F. Niekieł, L. Wondraczek, E. Spiecker, *Acta Materialia*, 79 (2014) 363-373.
- [7] M. Mačković, F. Niekieł, L. Wondraczek, E. Bitzek, E. Spiecker, *Scripta Materialia*, 121 (2016) 70-74.
- [8] H. Zheng, Y. Liu, S.X. Mao, J. Wang, J.Y. Huang, *Sci Rep*, 2 (2012) 542.
- [9] S.H. Li, W.Z. Han, Z.W. Shan, *Acta Materialia*, 141 (2017) 183-192.
- [10] J. Su, X. Zhu, *RSC Advances*, 7 (2017) 43047-43051.
- [11] J. Su, X. Zhu, *RSC Adv.*, 7 (2017) 45691-45696.
- [12] W. Stober, A. Fink, *Journal of Colloid and Interface Science*, 26 (1968) 62-69.
- [13] J. Kim, H. Woo, K. Joo, S. Tae, J. Park, D. Moon, S.H. Park, J. Jang, Y. Cho, J. Park, H. Yuh, G.D. Lee, I.S. Choi, Y. Nanishi, H.N. Han, K. Char,

- E. Yoon, *Sci Rep*, 3 (2013) 3201.
- [14] S. Yu, T.K.S. Wong, X. Hu, K. Pita, *Journal of The Electrochemical Society*, 150 (2003) F116-F121.
- [15] A.T. Nguyen, C.W. Park, S.H. Kim, *Bulletin of the Korean Chemical Society*, 35 (2014) 173-176.
- [16] J.S. Tse, D.D. Klug, Y.L. Page, *Physical Review B*, 46 (1992) 5933-5938.
- [17] T. Deschamps, A. Kassir-Bodon, C. Sonnevile, J. Margueritat, C. Martinet, D.d. Ligny, A. Mermet, B. Champagnon, *J Phys Condens Matter*, 25 (2013) 025402.
- [18] G. Kermouche, G. Guillonneau, J. Michler, J. Teisseire, E. Barthel, *Acta Materialia*, 114 (2016) 146-153.
- [19] Y. Tian, J. Du, D. Hu, W. Zheng, W. Han, *Scripta Materialia*, 149 (2018) 58-61.
- [20] J. Paul, S. Romeis, M. Mačković, V.R.R. Marthala, P. Herre, T. Przybilla, M. Hartmann, E. Spiecker, J. Schmidt, W. Peukert, *Powder Technology*, 270 (2015) 337-347.
- [21] R.F. Egerton, P. Li, M. Malac, *Micron*, 35 (2004) 399-409.
- [22] N. Jiang, *Rep Prog Phys*, 79 (2016) 016501.
- [23] Y.I. Golovin, A.I. Tyurin, V.V. Khlebnikov, *Technical Physics*, 50 (2005) 479-483.
- [24] A.A. Elmustafa, S. Kose, D.S. Stone, *Journal of Materials Research*, 22 (2011) 926-936.

- [25] R. Limbach, B.P. Rodrigues, L. Wondraczek, *Journal of Non-Crystalline Solids*, 404 (2014) 124-134.
- [26] D. Pan, A. Inoue, T. Sakurai, M.W. Chen, *Proc Natl Acad Sci U S A*, 105 (2008) 14769-14772.
- [27] E.V. Boltynjuk, D.V. Gunderov, E.V. Ubyivovk, M.A. Monclús, L.W. Yang, J.M. Molina-Aldareguia, A.I. Tyurin, A.R. Kilmametov, A.A. Churakova, A. A.Y. Churyumov, R.Z. Valiev, *Journal of Alloys and Compounds*, 747 (2018) 595-602.
- [28] H. Conrad, *Materials Science and Engineering A*, A341 (2003) 216-228.
- [29] I.C. Choi, Y.J. Kim, B. Ahn, M. Kawasaki, T.G. Langdon, J.I. Jang, *Scripta Materialia*, 75 (2014) 102-105.
- [30] A.A. Elmustafa, D.S. Stone, *Journal of Materials Research*, 22 (2011) 2912-2916.
- [31] L. Levien, C.T. Prewitt, D.J. Weidner, *American Mineralogist*, 65 (1980) 920-930.
- [32] J.S. Tse, D.D. Klug, *Phys Rev Lett*, 67 (1991) 3559-3562.
- [33] N. Binggeli, J.R. Chelikowsky, *Phys Rev Lett*, 69 (1992) 2220-2223.
- [34] X. Zhang, C.K. Ong, *Physical Review B*, 48 (1993) 6865-6870.
- [35] S. Subramanian, S. Yip, *Computational Materials Science*, 23 (2002) 116-123.
- [36] G.N. Greaves, A.L. Greer, R.S. Lakes, T. Rouxel, *Nat Mater*, 10 (2011) 823-837.

- [37] R.M. Wentzcovitch, C.d. Silva, J.R. Chelikowsky, *physical Review Letters*,  
80 (1998) 2149-2152.
- [38] M. Heggie, M. Nylén, *Philosophical Magazine B*, 50 (2006) 543-555.



## Chapter 4

### Total conclusion

Ceramic materials have been mechanically hard to handle owing to the low ductility and brittle fracture. Despite the ceramic materials have become essential elements of the construction, aerospace, automotive, optics, electronics industries due to their excellent thermal, corrosion, optical, and electrical properties, its low ductility and brittle nature complicate the fabrication process and cause questions constantly about mechanical reliability of the ceramic-based structural materials. High temperature above 1000 °C are essential for fabrication processes of the ceramic structural materials such as glasswork and sintering, and it is not easy to fabricate complex geometries through these processes. In addition, during the fabrication processes, internal flaws are spontaneously generated, and the fracture strength is highly dependent on these flaws. Therefore, it is always an important issue to secure mechanical reliability through the flaw control during the fabrication process, flaw distribution analysis, and the fracture strength evaluation.

Ceramic nanomaterials also cannot escape from these scientific and engineering issues. Recent researches have proposed the possibility of utilizing the ceramic nanomaterials with superior physical properties as a biomaterial,

energy material, and a constituent of the advanced electronic devices. However, concerns about the mechanical reliability of the ceramic nanomaterials have prevented a lively discussion on the practical applications of the ceramic nanomaterials. Although the size-related phenomenon of “smaller is stronger” recently have been reported, these results exclude the consideration of nano-flaws within the ceramic nanomaterials. In addition, some researches on the ductile deformation behavior of the amorphous silica under the irradiation of the high energy E-beam had been reported, and it was expected that it would be a breakthrough in the fabrication process field. Nevertheless, rigorous study on the E-beam induced deformation behavior of the ceramic nanomaterials including amorphous and crystalline phase is still lacking. In this research, the fracture strength of the ceramic nanomaterials with nano-flaws and the ductile deformation behavior induced by the E-beam irradiation were investigated.

Firstly, the fracture strength of the ceramic nanostructures which possess multiple nanopores was evaluated. A ceramic based hollow nanoshell structure which have been proposed as an interlayer structure of the GaN LEDs were fabricated through a series of processes using photolithography, atomic layer deposition, and appropriate heat treatment. The fabricated nanoshell structures contained multiple spherical nanopores with internal diameters of 20-32 nm and exhibited a porosity of about 5 % regardless of the nanoshell thickness. By systematically performing in-situ mechanical testing and finite element simulations, it was found that the fracture strength is about four times higher

than that of the conventional bulk  $\alpha$ -alumina even though the nanoshell structure contains a significant number of nanopores. Moreover, the high fracture strength of the  $\alpha$ -alumina nanoshell structure can be explained in the point view of the conventional fracture mechanics. With this high fracture strength, the applicability of the nanoshell structure as the interlayer of the GaN LEDs was investigated through the finite element analysis. It was confirmed that the residual thermal stress of GaN thin film is successfully mitigated when the nanoshell structure is applied, and most importantly the mechanical reliability can be secured, with a factor of safety of about 10, owing to the high fracture strength of the nanoshell. Based on the mechanical robustness of the nanoshell structure, actual GaN LEDs with  $\alpha$ -alumina nanoshell structure were fabricated with success, and exhibited an improved output power that is 2.2 times higher than that of conventional GaN LEDs.

Secondly, the ductile deformation behavior of ceramic nanomaterials induced by the E-beam irradiation was explored. It was found that the low energy E-beam obviously initiates the mechanical softening and plastic deformation of the amorphous silica. Moreover, there were the dependencies of the E-beam induced deformation behavior on the acceleration voltage and the beam current of the E-beam. With computational analysis, it is confirmed that this electron-beam effect strongly depends on the interacting volume between the incident electrons and the material. Moreover, this e-beam induced deformation behavior was also found in the other amorphous ceramic materials

including  $\text{Al}_2\text{O}_3$  and  $\text{TiO}_2$ . The e-beam induce deformation behavior of the amorphous ceramics was similar with the thermally activated homogeneous shear flow. In that, it can be deduced that the incident electrons into the material directly affect the interatomic bond nature, and a deformation behavior mimicking the thermally activated homogeneous shear flow emerges under the E-beam irradiation. For the crystalline ceramics, only the  $\text{SiO}_2$  shows the E-beam induced deformation behavior, because of its unique atomic structure where the amorphization occurs under pressure. Under the E-beam irradiation, the amorphization threshold pressure of the crystalline  $\text{SiO}_2$  decreases, and the amorphized  $\text{SiO}_2$  deforms further. Based on the E-beam induced ductile deformation behavior of the ceramic materials, a glasswork, normally conducted at high temperature for bulk scale, was performed inside the SEM. This “Nano-glasswork” was successfully demonstrated by forming the silica nanoshell structure in three different ways (simple uniaxial loading, multi-axial loading, and molding into the trench).

From this research, fundamental understandings of the fracture strength and the deformation behavior of the ceramic nanomaterials were established. Through the comprehensive study on the fracture strength, it is expected that an invaluable baseline for the design of 3D ceramic nanostructures in advanced devices will be provided. Moreover, an in-depth understanding of the ductile deformation of the ceramic nanomaterials induced by the E-beam irradiation will be a stepping stone for advanced manufacturing process for ceramic

nanomaterials. It is believed that this research will provide a breakthrough in the research on the ceramic structural nanomaterials and pioneer new fields in the fabrication processes and applications for ceramic structural nanomaterials.

The materials in Part 2 are reproduced with permission from “Flaw-Containing Alumina Hollow Nanostructures Have Ultrahigh Fracture Strength To Be Incorporated into High-Efficiency GaN Light-Emitting Diodes” Copyright 2018 American Chemical Society.

## 국문 초록

세라믹 재료는 금속, 비금속 혹은 준금속 간의 이온 결합 및 공유 결합으로 이루어진 화합물이다. 세라믹 재료는 우수한 열, 부식, 광학 및 화학 특성을 바탕으로 건설, 우주항공, 자동차, 광학, 그리고 전자산업의 필수요소로 자리잡아왔다. 하지만, 세라믹 재료의 낮은 연성과 소성변형이 없는 취성 파괴 때문에 구조 재료의 제조 공정이 복잡하고, 기계적 신뢰성에 대한 염려가 지속적으로 제기되어 왔다. 세라믹 구조 재료의 제작은 고온 조건이 필수적이며, 유리 가공이나 소결과 같은 제조 공정을 거쳐야하기 때문에 복잡한 구조를 제조하기에 적합하지 않다. 또한, 공정 중에 재료 내부에서 자연적으로 생성되는 결함은 구조 재료의 파괴 강도를 줄이고 기계적 신뢰성에 대한 우려를 불러일으킨다.

최근 구조 재료의 제조 기술이 향상됨에 따라 우수한 물리적 특성을 지닌 세라믹 나노 재료가 에너지 재료 및 첨단 전자 기기 분야에서 많은 주목을 받고 있다. 그러나, 세라믹 재료의 낮은 연성과 취성 파괴는 나노 스케일에서도 기계적 성질과 관련된 과학적 및 공학적 문제를 불러일으키고 있으며, 실용적인 응용에 대한 활발한 논의를 방해하고 있다. 최근, 세라믹 나노 재료의

크기가 작아짐에 따라 강도가 증가하는 현상이 보고된 바 있으나 이전의 연구에서는 재료 내부의 결함을 고려하지 않은 채 논의가 이뤄졌다. 또한, 고에너지 전자빔 조사 조건 하에서 비정질 실리카의 전례 없는 소성변형 현상이 보고되어 세라믹 재료의 제조 공정의 돌파구를 마련할 수 있을 것이라 예상되었지만, 다른 세라믹 재료에의 영향과 다양한 조건의 전자빔 조사 시의 변형 거동 변화와 같은 포괄적인 연구가 진행되지 않았다. 따라서 본 연구에서는 나노 결함을 포함하는 세라믹 나노 재료의 파괴 강도와 전자빔 조사 조건 하에서 나타나는 세라믹 나노 재료의 소성 변형 거동에 대한 연구를 수행하였다.

첫째, 다수의 나노 기공을 포함하는 세라믹 나노 구조체의 파괴 강도를 평가하였다. 세라믹 기반의 나노셀 구조체는 GaN계 발광다이오드(LED) 내 GaN 박막의 잔류 열응력을 완화시키고 소자의 효율을 향상시킬 수 있기 때문에, LED의 층간 구조로서 각광받고 있다. 그러나 내부에 다수의 나노 기공을 포함하는 나노셀 구조체가 GaN 박막의 잔류 열응력에 노출되었을 때, 기계적 신뢰성을 보장할 수 있는지에 대한 질문이 제기되어 왔다. 이에 본 연구를 통해  $\alpha$ -알루미나 나노셀 구조체를 제작하였고, in-situ 물성 평가 시스템 및 유한 요소 시뮬레이션을 통해 구조체의 파괴강도를

정량화하였다. 나노셀 구조체는 약 5%의 기공률을 보임에도 불구하고 기존 벌크 재료 대비 4배에 달하는 16 GPa의 파괴강도를 갖는 것으로 평가되었다. 뿐만 아니라, 나노셀 구조체의 크랙 형성 조건이 기존의 파괴 역학으로 설명 가능함을 보였다. 나노셀 구조체의 파괴강도에 대한 근본적인 이해를 바탕으로 유한 요소 시뮬레이션을 통해  $\alpha$ -알루미나 나노셀 구조체의 GaN LED에의 적용가능성을 조사하였다. 기존 연구결과들과 같이 나노셀 구조체가 적용될 때 GaN 박막의 잔류 열응력이 완화됨을 확인할 수 있었다. 가장 중요한 것은, 높은 파괴강도를 바탕으로 나노셀 구조체가 충분한 기계적 신뢰성을 보장할 수 있음을 확인한 점이다. 이를 바탕으로 실제 나노셀 구조체가 적용된 GaN LED를 제작하였고, 기존 GaN LED보다 약 2.2배 향상된 출력을 확인하였다.

둘째, 전자빔에 의한 세라믹 나노 재료의 소성변형 거동을 조사하였다. 지금까지의 연구결과들과 달리, 저에너지 전자빔 (수keV~ 수십keV)에 의한 세라믹 나노 재료의 기계적 성질 변화와 이 현상과 전자빔 파라미터(가속 전압, 빔 전류)와의 상관관계에 대해 연구하였다. 비정질 실리카의 소성변형 현상은 주사전자현미경 수준의 저에너지 전자빔 조건에서도 나타나는 것을 확인하였다. 재료 내에 입사한 전자의 에너지 변화와 이동경로를 모사하는



몬테-카를로 시뮬레이션을 통해 전자빔에 의한 변형 거동 변화 현상이 입사 전자와 재료 사이의 상호작용 부피에 크게 의존한다는 것을 유추할 수 있었다. 또한, 전자빔에 의한 변형 거동 변화 현상은 비정질 알루미나( $\text{Al}_2\text{O}_3$ ) 및 타이타니아( $\text{TiO}_2$ )에서도 동일하게 확인되었다. 비정질 세라믹 재료가 전자빔 조사 조건 하에서 보이는 변형 거동은 열적으로 활성화되는 전단 흐름(thermally activated shear flow) 변형 메커니즘과 상당히 유사하다. Thermally activated shear flow의 핵심 메커니즘은 지속적으로 변화하는 원자간 결합이다. 입사하는 전자의 에너지는 원자간 결합에 영향을 주기에 충분하기 때문에, 전자빔 조사 조건 하에서 소성변형이 나타나는 것이라 추론할 수 있다. 결정질 세라믹 나노 재료의 경우, 결정질  $\text{SiO}_2$ 의 독특한 원자구조 덕분에 유일하게 전자빔에 의한 변형 거동 변화 현상을 관찰할 수 있었다. 압축 응력 하에서 보이는 결정질  $\text{SiO}_2$ 의 비정질화 현상으로 인해, 전자빔 조사 시 비정질화를 위한 임계 응력 감소와 비정질화된 영역의 소성변형이 나타난다. 마지막으로, 나노 세라믹 재료의 소성변형 현상을 바탕으로 새로운 세라믹 구조재료 제작 공정을 제안하였다. “나노 유리세공”이라고 불리는 이 제작 공정은 비정질 세라믹을 주사전자 현미경 내에서 변형시키면서 원하는 형상으로 만드는

공정이다. 구형의 비정질 실리카 나노셀을 다양한 방법으로 변형시키면서 나노 유리세공 공정의 가능성을 확인하였다.

이 연구를 통해, 세라믹 나노 재료의 파괴 거동과 변형 거동에 대한 근본적인 이해가 확립되었다. 파괴 강도에 대한 포괄적인 연구가 최신 전자 기기에서 3차원 세라믹 나노 구조체의 설계에 대한 중요한 가이드라인을 제공할 수 있을 것이라 기대한다. 또한, 전자빔 조사에 의한 세라믹 나노 재료의 변형 거동 변화, 특히 소성 변형 현상에 대한 심층적인 이해는 세라믹 나노 재료의 첨단 제조 공정 개발을 위한 주춧돌이 될 것이라 예상한다. 본 연구가 세라믹 나노 재료의 기계적 특성 연구에 획기적인 진전을 가져오고 제조 공정 및 실제 응용 분야에서 새로운 분야를 개척할 수 있는 원동력을 제공할 것이라 기대한다.

**핵심어:** 세라믹, 나노 구조체, 나노 기공, 파괴강도, 크기효과, 파괴 역학, 기계적 신뢰성, 소성변형, 기계적 연화, 전자빔, 탄성/비탄성 산란, in-situ 나노 물성평가 시스템, SEM, FIB, TEM, 유한 요소 시뮬레이션, 몬테-카를로 시뮬레이션, LED, 가공성

**Student number:** 2013-20578